Engineering Structures 340 (2025) 120758

Contents lists available at ScienceDirect

Engineering Structures

journal homepage: www.elsevier.com/locate/engstruct

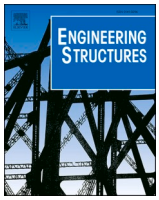

Redistribution of internal forces in masonry walls: A study through full-scale experiments and numerical simulations

Krzysztof Grzyb [a,*], Yiwei Hua [b], Radosław Jasiński [a], Gabriele Milani [b]

[a] Department of Building Structures, Silesian University of Technology, Akademicka 5 street, Gliwice 44-100, Poland
[b] Politecnico di Milano, Department of Architecture, Built Environment and Construction Engineering, Milano 20133, Italy

ARTICLE INFO

Keywords:
Masonry
Building
Shear walls
Stiffening walls
Internal forces
Redistribution
Stiffness
Crack
DIC
FEM

ABSTRACT

Stiffness is the key factor influencing force distribution within the structure. As lateral loads increase in buildings, cracking occurs, changing the values of internal forces. This phenomenon, known as the redistribution of internal forces, can be considered in calculations up to 15 % according to Eurocode 6, provided that the structure includes rigid floors capable of distributing the load to the stiffening elements. Nevertheless, the extent of the redistribution in masonry structures remains unrecognised in real-scale cases. This paper reports full-scale tests of three masonry buildings subjected to lateral loading with precompression. The process of crack propagation in masonry was captured using digital image correlation method. Nonlinear numerical analysis was also performed on a selected building with a door opening, which enabled changes in internal forces within the shear walls to be determined. This paper presents research on the lateral force redistribution phenomenon on stiffening walls and proposes a new analytical method for calculating internal forces based on experimental results. This method also allows for estimating the wall stiffness solely based on the known deformations of the building.

1. Introduction

Deep understanding and accurately predicting the behaviour of masonry is still an essential topic due to the widespread use of masonry structures, both historical and contemporary ones. Masonry as an anisotropic structure shows different properties depending on the direction considered [1]. The problem of analysing masonry as such is determined by various factors such as the heterogeneous nature of the two-phase material (construction made of masonry units and mortar [2]), quasi-brittle response in tension [3], geometric irregularities [4] and imperfections [5], strongly nonlinear response under loading and presence of openings in masonry. Moreover, the specimen size and the compressive strength ratio significantly impacted the shear strength of the masonry [6]. Some factors that complicate the considerations result from the material's properties and mechanical parameters, and others are directly concerned with the construction and the type of terrain on which the building is built. A systematic review of 54 selected articles [7] highlights disparities in experimental approaches and stresses the need for uniform testing procedures or standardisation protocol to ensure consistency and reliability.

Stiffness, both spatially and in terms of the stiffness of each structural element, is the most influential factor in force distribution within the structure. The load distribution or load-sharing among individual walls should be determined in the initial elastic phase of the building behaviour. As the load increases, progressive cracking changes the stiffness. The reduction in stiffness due to structural damage is called the stiffness degradation process. It is characterised by a disproportionate rise in deformation with an increase in the applied load. The redistribution of internal forces refers to the changes in internal forces within the structure caused by local weaknesses, such as cracking, plasticisation, or damage to load-bearing elements. This phenomenon depends on the relative stiffness of a particular part of the building. Due to degradation of stiffness, the rigidity of the walls changes, resulting in the transfer of loads to another, stiffer wall. This allows for partial maintenance of its load-bearing capacity and functionality despite the degradation of the primary elements.

The redistribution describes the differences between actual values of forces in correspondence to elastic values. Thus, considering the redistribution of internal forces resulting from cracking, the calculation results align more closely with the actual conditions of the structures. Unfortunately, this redistribution phenomenon in masonry is poorly described in the literature, and experimental studies are scarce. A few

* Corresponding author.
E-mail address: krzysztof.grzyb@polsl.pl (K. Grzyb).

https://doi.org/10.1016/j.engstruct.2025.120758
Received 27 February 2025; Received in revised form 24 May 2025; Accepted 5 June 2025
Available online 11 June 2025

studies describe load distribution in wood buildings [8,9] or load-sharing mechanisms in timber-steel systems [10]. There is also a study of seismic force distribution in confined masonry [11]. Most studies concern moment redistribution in statically indeterminate reinforced concrete beam systems [12–14], composite structures [15–18], or slabs [19–21]. Bending moments are transferred from yielding sections to elastic sections due to plastic rotations [22]. Taking into account moment redistribution during the structural design process is an effective method for exploiting the reserve load-bearing capacity of construction. This approach can lead to more efficient and cost-effective construction projects and improved overall structure performance. In engineering practice, considering the redistribution of internal forces in continuous beams involves calculating internal forces using linear elasticity theory, followed by their multiplication by the redistribution factor. This method, known for its simplicity and practicality, accurately reflects specific characteristics of structural nonlinearity. Redistribution is significant in construction connections. Three full-scale composite beams were tested at the Institute of Structural Concrete of the RWTH Aachen University to observe a redistribution of shear forces along the interface from the regions with cracked concrete to regions with uncracked concrete. It has been proven that the high ductility of the dowels in cracked concrete was found to counteract their reduced resistance by allowing a shear-force redistribution along the composite interface [23]. Furthermore, in a shear field with multiple dowels located partially in cracked and partially in uncracked concrete, the diminished stiffness of the dowels in the damaged concrete area was shown to facilitate the redistribution of the shear loading towards the stiffer dowels in the undamaged, compressed concrete. It was suggested that a "per-shear field" design approach can be more realistic and economical than an approach based on "per-dowel".

A redistribution phenomenon also occurs in masonry stiffening walls parallel to the load direction. However, it should be noted that masonry structures crack under lower loads than reinforced concrete structures, meaning that redistribution occurs much earlier in the structural system. The distribution of internal forces in a building is influenced by various factors, such as wall geometry – aspect ratio [24,25], openings [26–31], type of slabs [32] either rigid diaphragm or flexible [33–35], the direction of slab support and initial compressive stresses concerned with vertical loads [36,37]. Considering a horizontal load applied at the building's centre of stiffness – which, for a model without window openings and with identical wall geometry, is situated at the geometric centre of the building – will result in a symmetrical distribution of the load (the internal forces of wall A and B will be the identical) – Fig. 1(a). At the elastic stage of structural behaviour, it is essential to consider the distribution of loads (load-sharing). After one of the walls cracks, its stiffness degrades, leading to a redistribution of internal forces. Consequently, the uncracked wall, having greater stiffness, will bear a larger portion of the load than the cracked wall – Fig. 1(b).

Eurocode 6 [38], dedicated to designing European masonry structures, includes a seemingly modest reference to redistributing internal forces. This provision is outlined in Section 7.6, which addresses flange widths that can be assumed for shear walls. Standard states: "*The maximum horizontal load on shear wall may be reduced by up to 15 % provided that global equilibrium is maintained*". It is worth noting here that the definition of a shear wall is a wall to resist horizontal forces in its plane. Sometimes, the concept of a stiffening wall is utilised. A stiffening wall can be defined as a wall set perpendicular to another wall to support it against horizontal forces or to resist buckling. In this work, these terms will be used interchangeably. The provision allowing for a 15 % reduction in the load distribution assigned to a given shear wall effectively permits design accounting for the redistribution of internal forces. Although Eurocode requires that loads be distributed to the stiffening

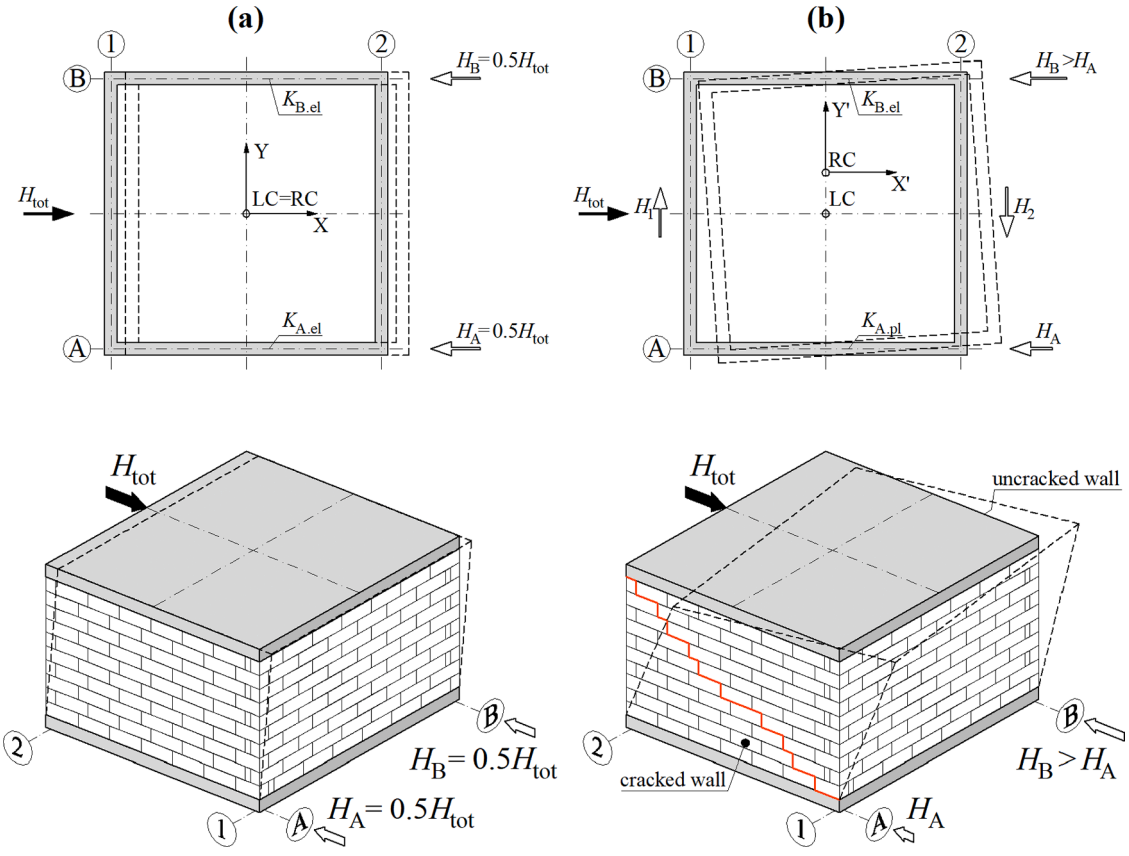

Fig. 1. Redistribution of internal forces in masonry building: (a) uncracked phase, (b) cracked phase, LC – load centre, RC – rotation centre, H_{tot} – total horizontal force, H_A, H_B – internal forces in stiffening walls, H_1, H_2 – internal forces in perpendicular walls, $K_{A.el}$, $K_{B.el}$ – elastic stiffness of stiffening walls, $K_{A.pl}$ – post-elastic stiffness of stiffening wall A (cracked).

elements in proportion to their stiffness in the case of rigid floors, it does not define how to calculate the stiffness of these elements or how to account for the redistribution of forces practically. These two premises constitute the primary motivation for the study: how to estimate the stiffness of walls and what the actual magnitude of the redistribution of internal forces is for a building subjected to horizontal loading. The article contributes to the development of knowledge by: consciously planned research addressing the issue of redistribution and identifying phenomena confirming the redistribution process occurring in masonry structures, along with a description of crack propagation and the increase in deformations. The work includes the results of full-scale masonry building models, a proposal for a simplified analytical method, the validation of the FEM model on a full-scale structure, and the determination of the level of redistribution of internal forces.

2. Materials and methods

2.1. Assumptions of research program

The presented research is part of an extensive program at The Silesian University of Technology at the Faculty of Civil Engineering involving analyses of full-scale models of unreinforced and confined masonry buildings subjected to monotonic horizontal loading. The studies available in the literature primarily concern single masonry walls subjected to cyclic loading. Moreover, the peculiarities of the stiffening walls demand an analysis of the cooperation with perpendicular walls, so-called flange walls. Flat models, although valuable, also do not provide the opportunity to analyse the torsion of the entire building, capturing the change in the values of internal forces in the walls due to the progressive degradation of masonry stiffness and the redistribution phenomenon. The above rationale demonstrates the need to fill this research and theoretical gap. The main assumptions of the research program can be summarised in the points below.

(a) The research models are unreinforced masonry, single-story buildings with a simple layout.
(b) The models are subjected to monotonic horizontal loading.
(c) Buildings are made of modern construction materials.
(d) Model building technology enables construction in the fastest way possible.
(e) The floor structure only acts as a rigid diaphragm to transfer horizontal loads to the walls.
(f) The test setup enables the initial compressive stresses to be applied to the walls.
(g) The boundary conditions of the tests correspond to actual buildings.

2.2. Building models

Each model is a building consisting of four masonry walls and a rigid floor. The walls parallel to the horizontal load direction are stiffening walls, and the other two are perpendicular. The building's horizontal layout dimensions are 4.0 × 4.0 m, and the total height is 2.85 m. The thickness of the wall is 18 cm. Models are marked with an alphanumeric symbol MB-AAC-010/N. MB stands for masonry building, while AAC refers to autoclaved aerated concrete, and N is the number of the tested building. The article presents research on three building models. Model 2, in which a door opening is made in one of the stiffening walls, and the

Table 1
List of tested building models.

Model designation/3D views		Wall	Opening	Description
MB-AAC-010/2	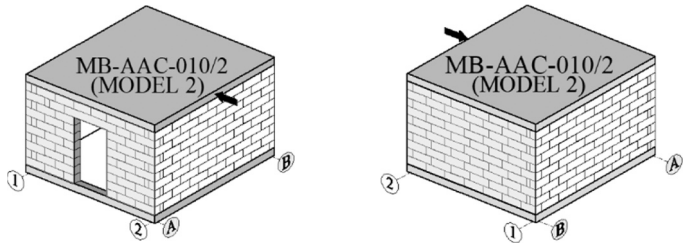	A	door opening	stiffening
		B	solid	
		1	solid	
		2	solid	perpendicular
MB-AAC-010/8	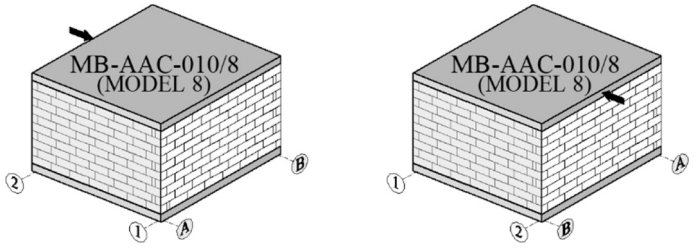	A	solid	stiffening
		B	solid	
		1	solid	
		2	solid	perpendicular
MB-AAC-010/9	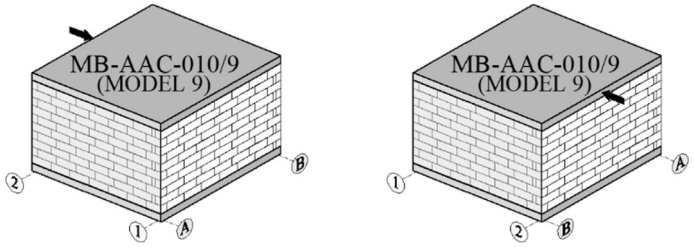	A	solid	stiffening
		B	solid	
		1	solid	
		2	solid	perpendicular

remaining walls are solid. Both models 8 and 9 are identical reference models without openings. The summary of models is shown in Table 1.

The walls of the models were constructed using autoclaved aerated concrete (AAC) masonry units. Each block measures 180 mm× 590 mm × 240 mm. The thickness of the building walls matches the width of the masonry block (180 mm). The walls were assembled with thin-joint mortar, and the bed joints were filled with mortar of class M5. The head joints were left unfilled, allowing the masonry units to connect through a tongue-and-groove design. The slab functioned as a rigid diaphragm in the tests, transferring horizontal loads to the building's masonry walls. It was designed for multiple uses, which helped to reduce the model's construction time. The process relied primarily on constructing new walls. To prevent the slab from slipping under applied horizontal loading, additional mechanical connectors in the form of long nails were used to ensure composite action between the two structural elements. The procedure for erecting successive models consisted of the following stages (Fig. 2):

1. Building the model.
2. Testing the building.
3. Cutting off the walls from the slab.
4. Lifting the slab on an overhead crane.
5. Laying the slab on assembly supports based on a steel structure.
6. Demolishing the walls of the tested building.
7. Constructing a new model of the building (new masonry walls).
8. Laying the slab.

2.3. Test stand for stiffening walls and measuring techniques

The test setup allowed vertical and horizontal loads to be applied to the tested structure. The research model was securely fixed to a strong floor. Restraint was achieved using additional horizontal beams that surrounded the bottom beam of the model, anchored to the laboratory floor with bolts measuring 65 mm in diameter. A steel column with a brace was positioned next to the model. The horizontal load was applied monotonically at the geometric centre of the slab, halfway along the masonry wall, using a 1500 kN actuator (force measurement using a 250 kN force gauge, class 1) supported by a steel structure mounted on the steel column. A vertical load was designed to correspond to the actual load on the building's slab, including the weight of the finishing layers and the live load. The weights with a diameter of 60 cm and a height of 30 cm were used to induce initial compressive stress in masonry walls. The vertical load was suspended on the twelve steel rods with a diameter of Ø16 mm, and three weights hung on each rod. The values of compressive prestress of the walls are $\sigma_c = 0.05$ N/mm^2. The building models at the test site are shown in Fig. 3.

The displacements were measured using a set of frame systems and linear variable differential transformer (LVDT) sensors. The frames attached to the tested building were rectangular, 3260 mm long, and 2150 mm high. LVDT sensors with a measuring range of 20 mm (PJX-20) were mounted diagonally, while LVDT sensors with a range of 10 mm (PJX-10) were installed on the vertical and horizontal frames. The resolution of the measurements was 0.005 mm. The shear deformation angle was calculated as the arithmetic mean of the partial values of the global shear deformation angle, which were determined based on changes in the lengths of the measurement bases [39]. The shear deformation angle of the walls should be interpreted as the structural deformation caused by the action of horizontal loading. Measurement bases are visible in photographs of models on the test stand – Fig. 3(c, d). The selected building areas were painted with a speckle pattern for the digital image correlation system – Fig. 3(b).

3. Results

3.1. Structural performance

The behaviour of the tested building models is presented in normalised graphs, where the vertical axis represents the ratio of the horizontal load H_i relative to its maximum value H_u, and the horizontal axis shows the value of the deformation angle Θ or horizontal displacement parallel to load u_x. The graphs were created for the stiffening walls A and B, and appropriate miniature models of the buildings were also included to enhance their clarity. In Figs. 4–6, the results of the tests for models 2, 8, and 9 are presented. The results given to three significant figures for each behaviour phase – initial, elastic, nonlinear, and residual [39] – are summarised in Table 2.

The initial phase occurs only in wall A with a door opening in building model 2. It concerns the first cracks in the tensioned corner of the opening at a low level of horizontal loading. This phenomenon is clearly visible thanks to the utilisation of digital image correlation (Fig. 8a). Wall A, with an opening, also has lower stiffness, resulting in greater deformations at every load level. In the elastic phase, the displacements of this wall are 2.4 times greater compared to the stiffening wall B without an opening ($\Theta_{cr.M2.A}/\Theta_{cr.M2.B} = 2.40$). At maximum loading, these values will be 2.5 times greater ($\Theta_{u.M2.A}/\Theta_{u.M2.B} = 2.50$). Only in the residual phase will the displacements of wall A exceed those of wall B by just 35 %. In the reference building models 8 and 9, without openings, the deformation values should theoretically be the same throughout the entire loading process. Actually, cracking occurs first in one of the walls, and it is in this wall that greater deformations will be observed before cracking occurs in the second wall. This effect was most clearly visible in model 9, wherein the elastic phase, the deformations of wall A were 2.2 times greater than those of wall B. The deformations were equalised only in the residual phase. The deformation values were similar at maximum loading and in the residual phase ($\Theta_{u.M9.A}/\Theta_{u.M9.B}$

Fig. 2. Procedure for building models: (a) cutting off the walls from the slab, (b) demolishing the walls of a previously tested model with visible concrete weights designed to induce initial compressive stresses in the walls.

Fig. 3. Building models on the test site: (a) construction of the foundation for masonry walls, (b) model 2 with visible steel column and hydraulic actuator, (c) corner view of model 8, (d) stiffening wall view of model 9. 1 – reinforcement of foundation, 2 – extra concrete beams along the perimeter to guarantee the model remains fixed.

$= 0.98$ and ($\Theta_{res.M9.A}/\Theta_{res.M9.B} = 1.07$). In model 8, the deformation magnitudes were similar in the elastic ($\Theta_{cr.M8.A}/\Theta_{cr.M8.B} = 0.96$) and residual phases ($\Theta_{res.M8.A}/\Theta_{res.M8.B} = 1.12$). The most considerable discrepancies were observed at the maximum value of horizontal loading ($\Theta_{u.M8.A}/\Theta_{u.M8.B} = 1.63$). The moment of cracking in the structure and the consequences of the damage directly influences its structural behaviour. Another important factor affecting stiffness is the presence of openings in the walls.

3.2. Crack propagation

A digital image correlation system captured the initiation and propagation of cracks in the bed and head joints. The DIC method helps to identify the formation of cracks in early testing stages when the eye inspection cannot detect incipient damage. As indicated in Fig. 7, selected sections of the stiffening walls in the building models were analysed. Cracks in each wall exhibited a stepped pattern, corresponding to the typical failure mode due to in-plane shear under low initial

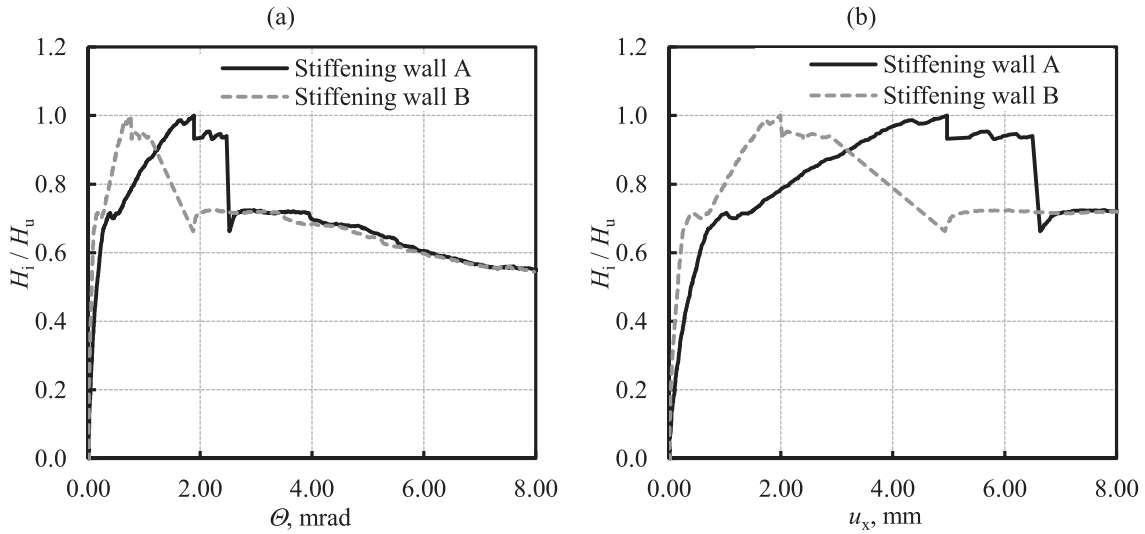

Fig. 4. Structural behaviour of model 2 based on stiffening walls analysis: (a) normalised horizontal load–deformation angle diagram, (b) normalised horizontal load–horizontal displacement.

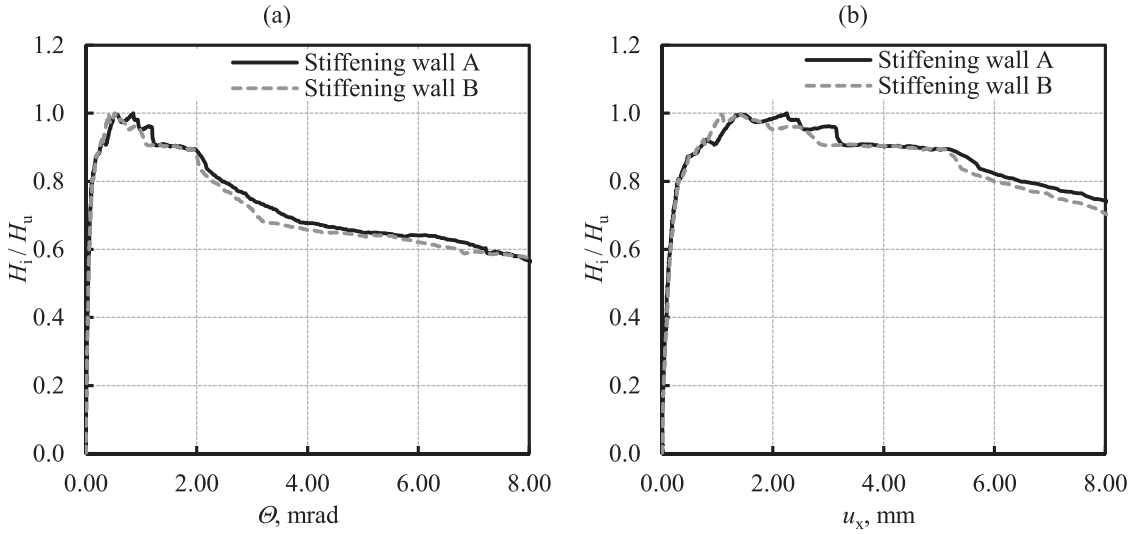

Fig. 5. Structural behaviour of model 8 based on stiffening walls analysis: (a) normalised horizontal load–deformation angle diagram, (b) normalised horizontal load–horizontal displacement.

compressive stresses (Figs. 8–10). In the wall with a door opening, the first crack appears at the tensile corner of the opening – Fig. 8(a), while in the solid walls, the crack initiates from the side where the load is applied – Fig. 9(a) and Fig. 10(a). An increase in horizontal loading causes the crack to propagate diagonally, dividing the stiffening masonry wall.

3.3. Damage pattern

The literature distinguishes three primary types of shear wall failure under horizontal loading and initial compression: flexural failure, shear-diagonal failure, and shear-sliding failure [40,41]. Based on full-scale studies, shear-diagonal failure was observed in stiffening walls A and B in models 2, 8, and 9 (Figs. 11–13). Such damage is related to the loss of bearing capacity in masonry panels due to excessive shear and the resulting formation of inclined diagonal cracks along the direction of principal stresses. There are two leading causes of this type of damage: the low level of compressive stresses and the geometry of the wall, which has been designed so that shear deformations are decisive.

The nature of the damage in the perpendicular walls 1 and 2 is different. In the wall to which the horizontal load was applied, a horizontal crack was observed in the bed joints at mid-height of the wall, resulting from its uplifting – Fig. 12(b) and Fig. 13(b). On the opposite wall, the loss of the bearing capacity is related to the crushing of the masonry in the compression zone. The damage resulting from excessive compression manifested as crushing of the masonry units e.g. Fig. 11(b).

4. Numerical simulations

This section presents the numerical simulation of the AAC masonry building with an opening (Model 2) to illustrate the feasibility of retrieving the internal forces, which are not accessible to the measurement in the experiment, through finite element analysis. The finite element model of this tested building is established in commercial software ABAQUS. The material parameters are first calibrated based on the load-displacement results from the experiment. Then, the deformation and crack propagation results will be compared to the experiment for verifying purposes, and the stress distribution of the system will also

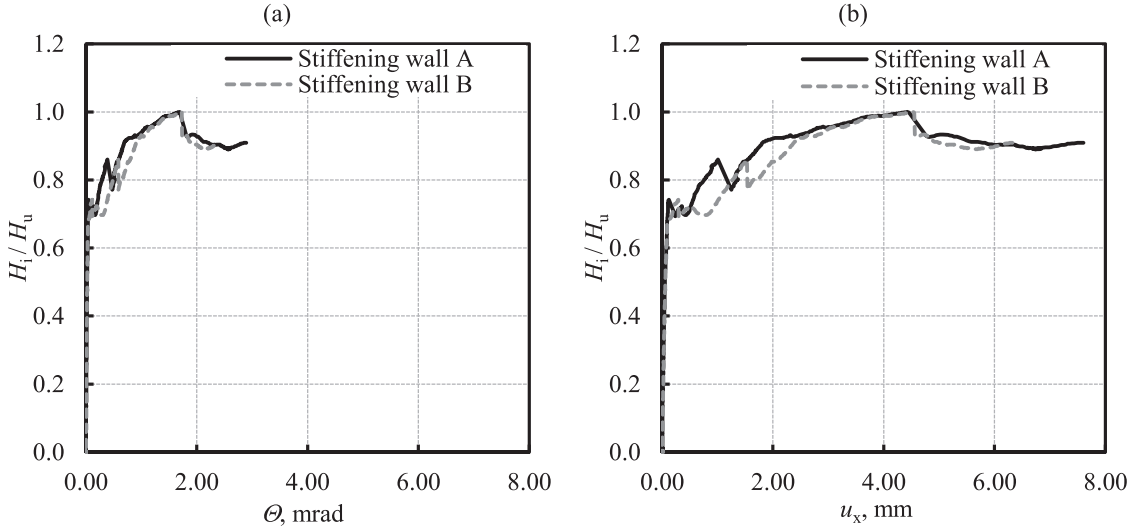

Fig. 6. Structural behaviour of model 9 based on stiffening walls analysis: (a) normalised horizontal load–deformation angle diagram, (b) normalised horizontal load–horizontal displacement.

Table 2
Summary of test results of models 2, 8, 9.

Model	Model wall	Initial phase		Elastic phase		Nonlinear phase		Post-peak residual phase	
		$H_{cr,1}$, kN	$\Theta_{cr,1}$, mrad	H_{cr}, kN	Θ_{cr}, mrad	H_u, kN	Θ_u, mrad	H_{res}, kN	Θ_{res}, mrad
2	A	9.76	0.0198	49.6	0.389	69.2	1.89	45.9	2.52
	B	-	-		0.162		0.756		1.87
	1	-	-		0.0271		0.183		0.131
	2	-	-		0.0289		0.136		0.160
8	A	-	-	52.9	0.114	65.5	0.856	59.3	1.28
	B	-	-		0.118		0.526		1.15
	1	-	-		0.00854		0.030		0.0312
	2	-	-		0.0242		0.135		0.0800
9	A	-	-	65.8	0.110	88.7	1.68	82.76	1.91
	B	-	-	60.6	0.0500		1.72		1.79
	1	-	-	38.2	0.0135		0.0651		0.0542
	2	-	-	60.6	0.0170		0.0278		0.0710

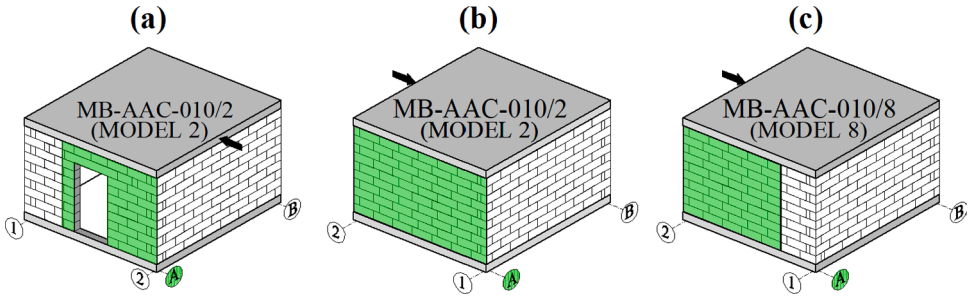

Fig. 7. The area analysed using the DIC method: (a) wall A of model 2, wall B of model 2, wall A of model 8.

be provided. The calibrated model will then be utilised to investigate the internal force of the walls in the discussion.

4.1. Finite element model and calibration

In the finite element model, the geometry of each AAC block is precisely considered, following the bond pattern employed in the corresponding experiment. Each masonry unit is considered elastic for the sake of simplification, with no plasticity or degrading feature, since the failure majorly takes place at the interfaces between the blocks in the experiment. Those mortar interfaces are modelled through cohesive-frictional contacts (realised through a combination of "*Hard contact*", "*Tangential friction*", "*Cohesive behaviour*", and "*Damage*" properties in ABAQUS). The post-peak softening characteristic of the contact in the normal direction is linear degradation controlled by the fracture energy, as illustrated in Fig. 14(a). The peak of the curve is the tensile strength of the mortar-AAC interface, and the enveloped area of this bilinear curve defines the fracture energy. These parameters are all available from the relevant material property test but require further calibration. The tangential sliding has a very similar characteristic to the normal behaviour but with the addition of a residual platform stage due to the presence of friction (Fig. 14(b)). The rest of the concrete components are

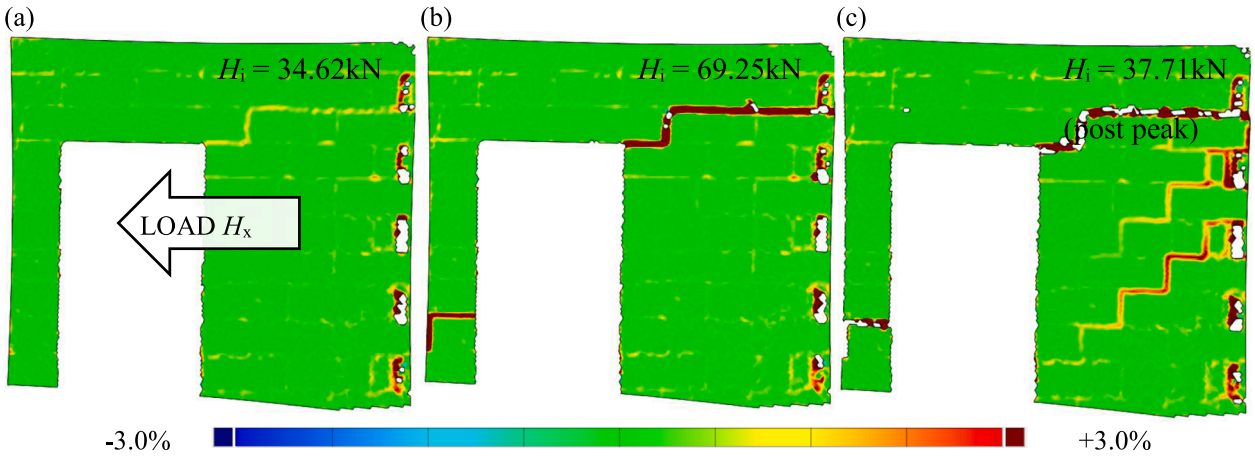

Fig. 8. Crack propagation in part of Wall A of Model 2: (a) crack pattern at H_i = 34.62 kN, (b) crack pattern at H_i = 69.25 kN, (c) post-peak crack pattern at H_i = 37.71 kN.

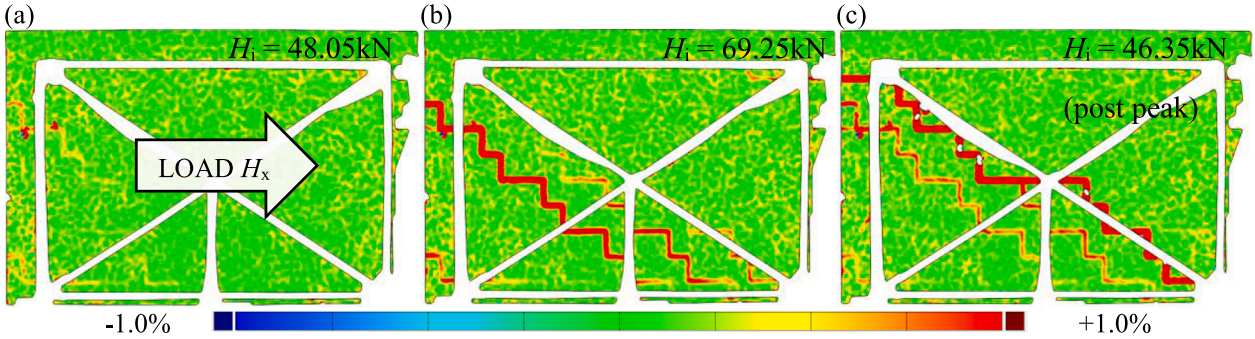

Fig. 9. Crack propagation in part of Wall B of Model 2: (a) crack pattern at H_i = 48.05 kN, (b) crack pattern at H_i = 69.25 kN, (c) post-peak crack pattern at H_i = 46.35 kN.

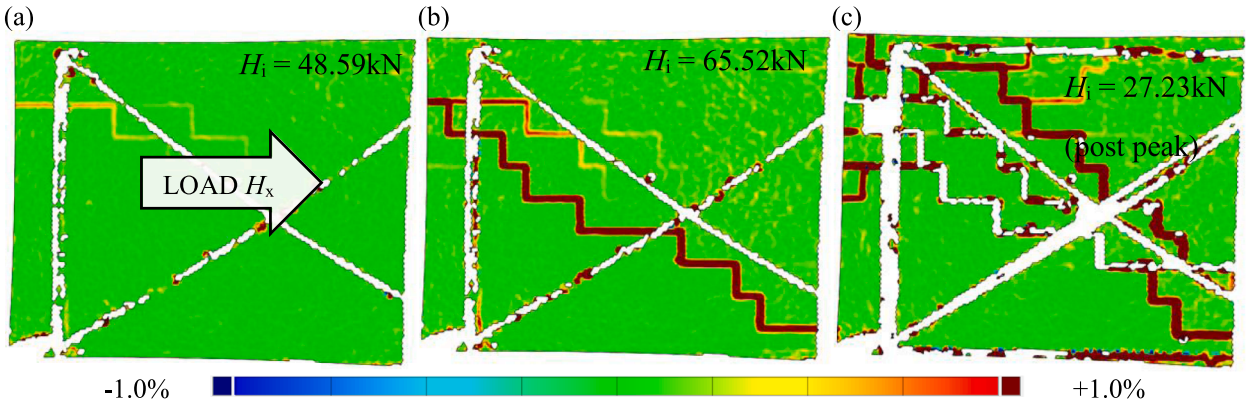

Fig. 10. Crack propagation in part of Wall A of Model 8: (a) crack pattern at H_i = 48.59 kN, (b) crack pattern at H_i = 65.52 kN, (c) post-peak crack pattern at H_i = 27.23 kN.

elastic as well. All the parameters initially obtained from the material property tests are provided in Table 3. Note that tongue-and-groove joints horizontally stack the blocks in each layer without using bonding material. A stronger frictional coefficient is thus assigned to those joints, whereas the cohesive-damage behaviour is not adopted.

To agree with the loading scheme of the experiment, the load step assigned in the simulation comprises three steps (Fig. 15(a)). The first step applies vertical gravity. Then, a surface pressure of 4.59kN/m^2 is imposed on the top slab as an equivalent of the dead load. After that, a lateral displacement-control pushover analysis is executed. The displacement is imposed at the middle of the side surface of the concrete slab, with a monotonic increase until the simulation is aborted due to loss of convergence. The structure is regarded as losing resistance at this stage. The structure is considered to lose resistance when the procedure is aborted due to a loss of convergence. All the bottom nodes of the concrete beam support are fixed to represent the boundary condition in the test experiment. The mesh of the model adopted in the simulation is given in Fig. 15(b).

A reasonable estimation of the properties for the units and interfaces of Model 2 must be conducted, which could be done by calibrating the peak load. Additionally, because of the dimension effect, the material property obtained from the small-scale test could not precisely represent

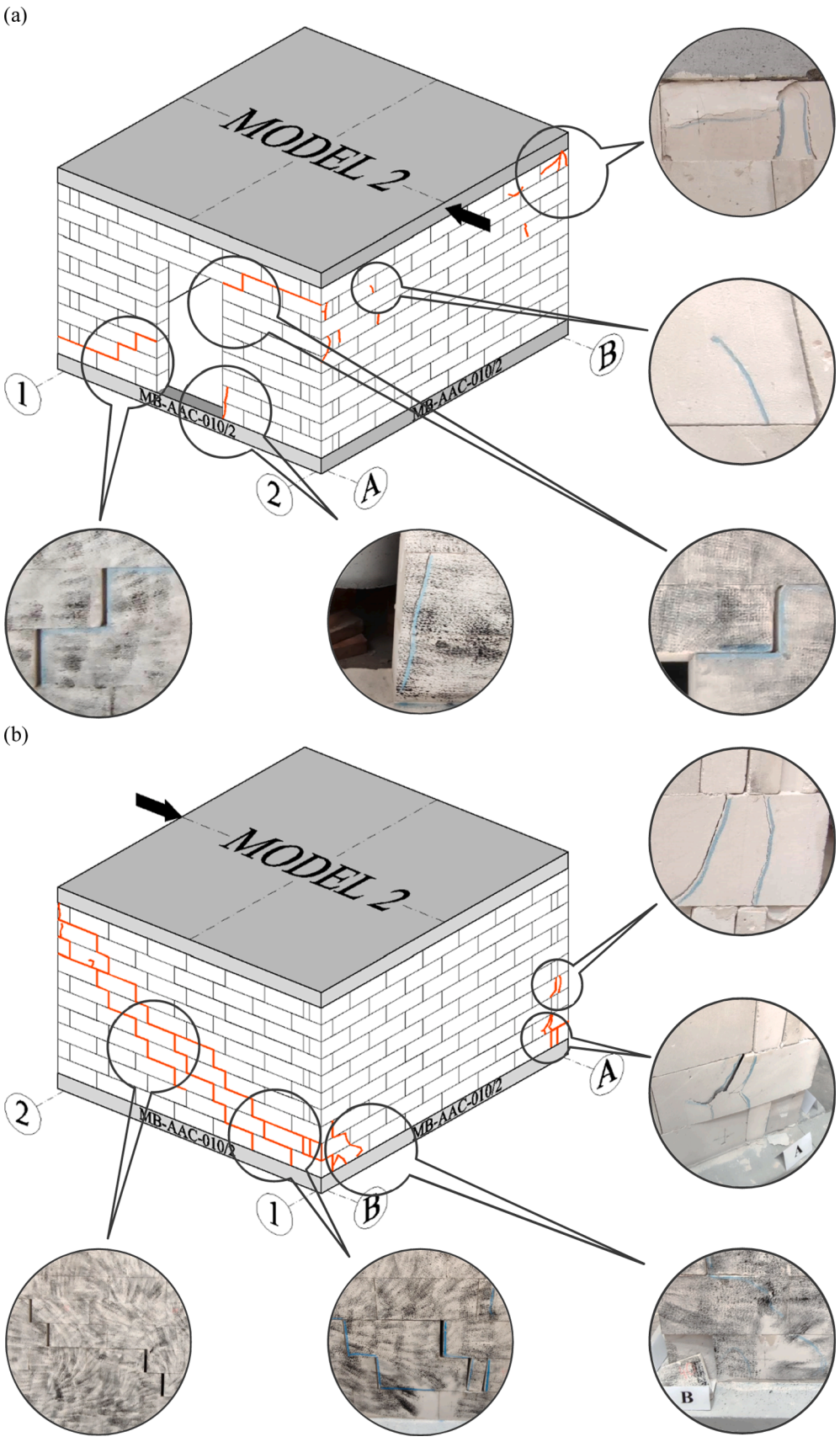

Fig. 11. Damage pattern of building model 2: (a) stiffening wall A with a door opening and solid wall 2, (b) solid stiffening wall B and solid wall 1.

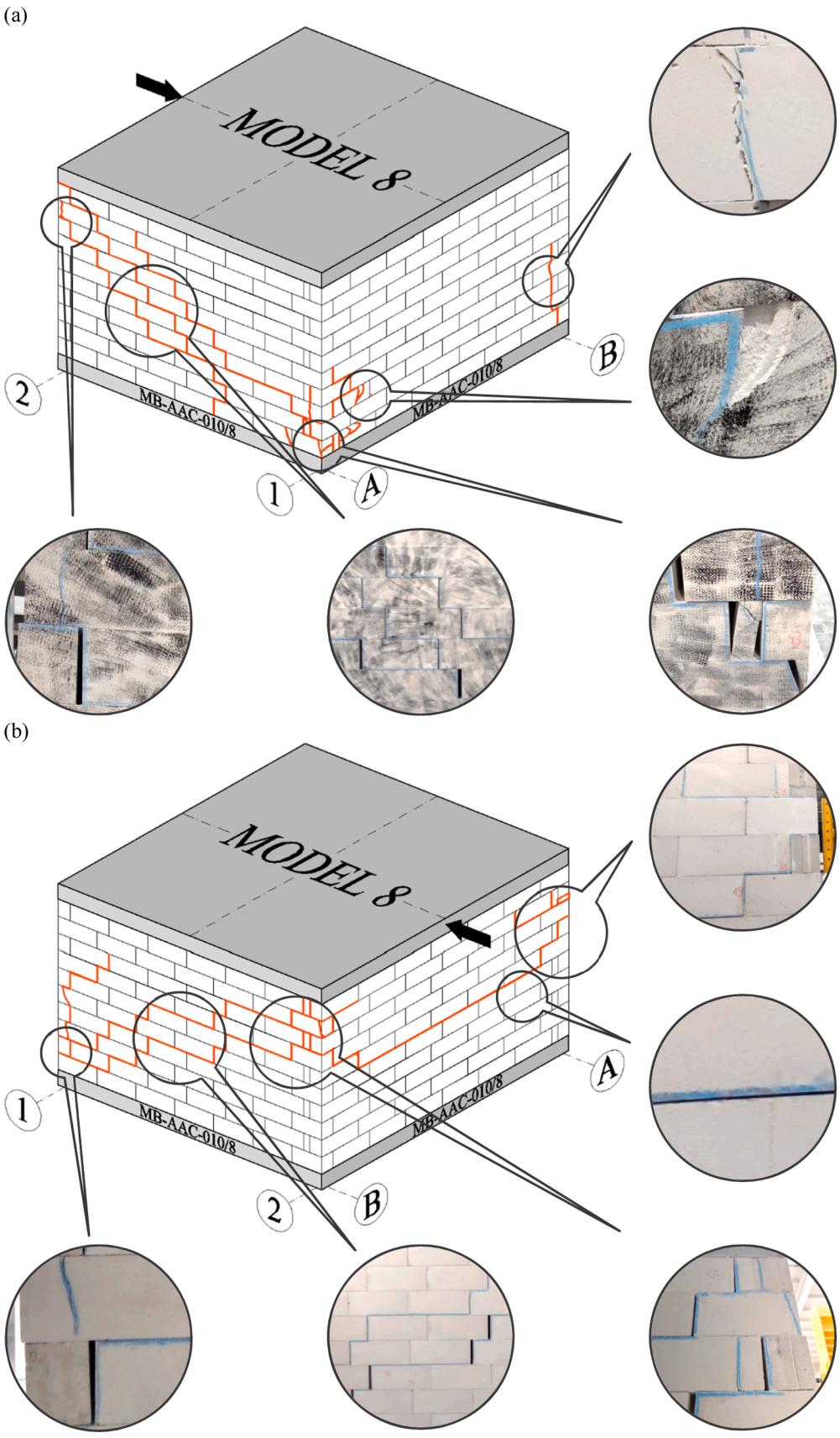

Fig. 12. Damage pattern of building model 8: (a) solid stiffening wall A and solid wall 1, (b) solid stiffening wall B and solid wall 2.

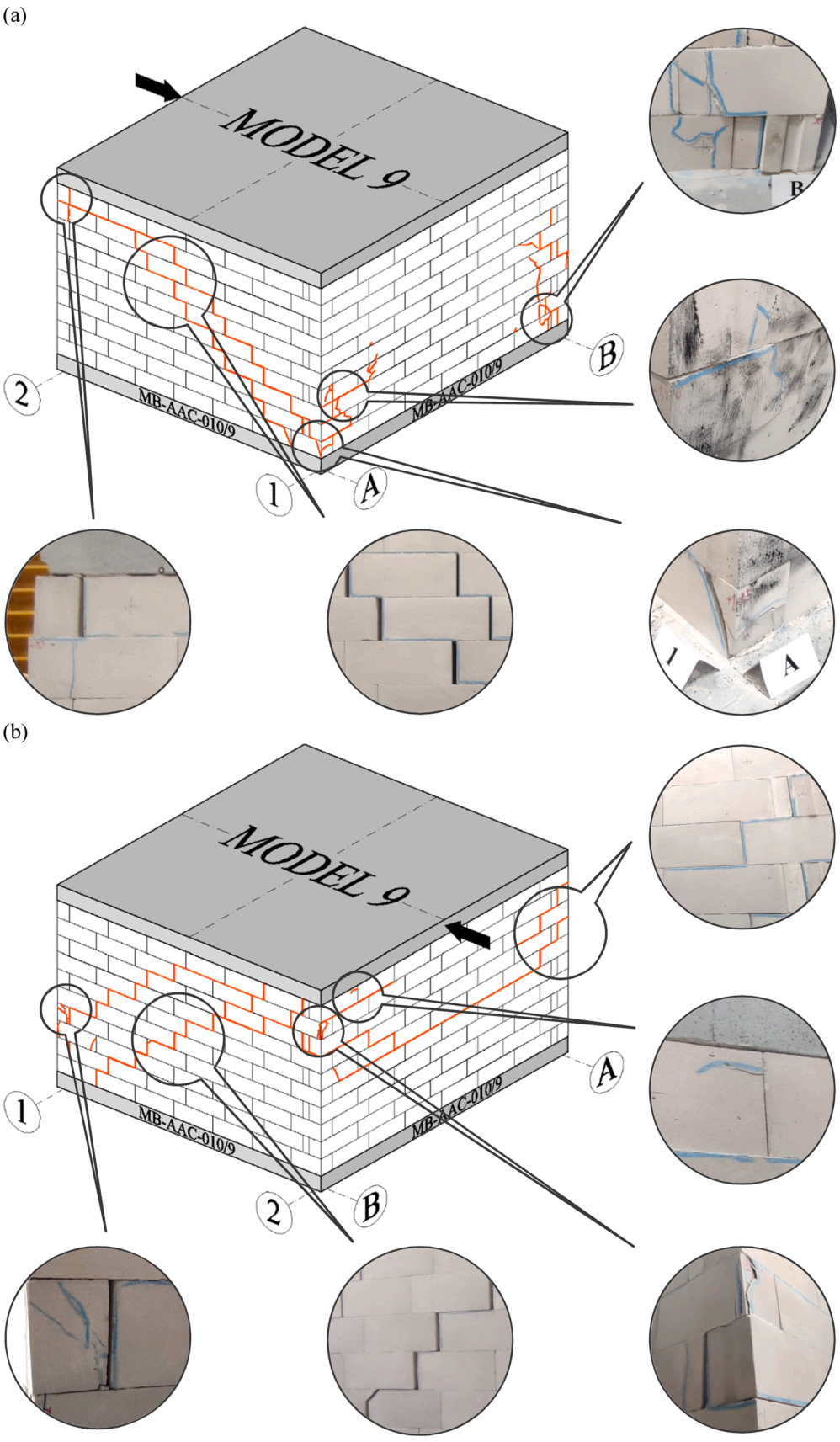

Fig. 13. Damage pattern of building model 9: (a) solid stiffening wall A and solid wall 1, (b) solid stiffening wall B and solid wall 2.

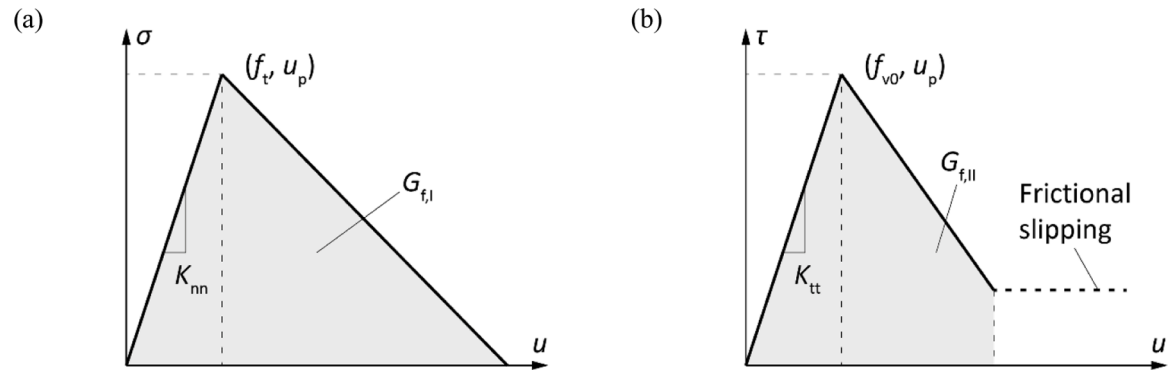

Fig. 14. Interfacial constitutive model for the bed joint: a) normal behaviour; b) tangential behaviour.

Table 3
Material parameters used for the numerical analysis and the calibrated value.

Parameter		Unit	Value	Calibration factor	Calibrated value
Concrete	Elastic modulus E_c	MPa	30,000	1	30,000
	Poisson ratio ν_c	-	0.2	1	0.2
	Density ρ_c	kg/m^3	1580	1	1580
AAC units	Elastic modulus E_b	MPa	2204	0.23	506.92
	Poisson ratio ν_b	-	0.131	1	0.131
	Density ρ_b	kg/m^3	600	1	600
Horizontal Joint (Bed joint)	Normal stiffness K_{nn}	MPa/mm	18,888.9	0.001	18.889
	Tangential stiffness K_{tt},	MPa/mm	8351.87	0.001	8.352
	Tensile strength f_t	MPa	0.29	0.143	0.0414
	Cohesion f_{vo}	MPa	0.31	0.143	0.0443
	Friction coefficient	-	0.454	0.771	0.35
	Fracture energy G_{fII},	N/mm	0.237	0.422	0.1
Vertical Joint (Head joint)	Normal stiffness K_{nn}	MPa/mm	18,888.9	0.001	18.889
	Tangential stiffness K_{tt},	MPa/mm	8351.87	0.001	8.352
	Friction coefficient	-	0.817	1	0.817

its behaviour at the structural level. Direct usage of these parameters may be inaccurate when executing the structural-level simulation. Since the peak load of Model 2 is about 23 % of that of the sample building, with relevant material tests conducted. The basic reduction factor is set as 0.23, which first applies to the AAC elastic modulus. The interfacial stiffness parameters from the test are quite high, possibly because the scale effect was ignored. These parameters are thus scaled down considering the real stiffness magnitude of the mortar joint. Due to the lack of tests for AAC-to-AAC interfaces, we take the brick-to-brick mortar interface as a reference, which usually ranges from 10^1 to 10^2 MPa/mm [42–45]. The scale factor is finally determined as 0.001. The reduction factors of other parameters are slightly adjusted around the fundamental value with several attempts to calibrate the peak load of the experiment. All these factors are listed in Table 3, and the parameter eventually employed in the numerical simulation is the value with scaling.

Fig. 16 gives the load-displacement curves of two stiffening walls in Model 2 after the calibration. The deviation of the total load is only about 5.8 %, indicating that the calibrated numerical model can represent the situation in the experiment. Consistent linear elastic, nonlinear increasing and post-peak softening behaviour are noted in the experimental curves. Slight deviation only appears at the curve of the solid stiffening wall, with a lag of the load drop in the numerical result. In general, it can be concluded that the information obtained from this twin model can retrospectively infer the behaviour of the experimental sample.

Observing the system dissipation in the numerical simulation helps us better understand what happens in the AAC wall in the test. Fig. 17 displays curves of the energy induced by the elastic deformation, interfacial elastic, interfacial damage, and interfacial friction, respectively. The elastic strain energy of the system is dominant in the linear increase stage of the load history. The following nonlinear stage happens due to the appearance of interfacial damage, and the cracks begin to evolve. In the latter half of this stage, the cohesive effect of some interfaces completely fails, and the frictional dissipation rises. The sudden interfacial sliding induces an abrupt drop in the load history since the friction dissipation correspondingly rises, which further releases the elastic strain energy in elements and interfaces. In the post-peak stage, the interfacial damage and frictional dissipation majorly contribute to the growth of the system energy.

4.2. Deformation and stress distribution

The overall deformation of the walls is given in Fig. 18(a). The whole building twists due to the asymmetric stiffness distribution. The lateral movement of the wall with the opening is larger than the solid wall because of its lower stiffness. Therefore, from the top of the view, the building slightly rotates towards the solid stiffening wall during the horizontal pushing (Fig. 18(b)). However, the difference between the deformation of the two stiffening walls closes after the solid stiffening wall cracks. The torsion effect thus almost vanishes in the post-peak stage of the loading (see the displacements listed in Table 4). The deformation of the two stiffening walls is basically in-plane. The out-of-plane deformation of the two perpendicular walls is almost the same. The lean of the perpendicular wall at the loading side is slightly higher.

Table 4 lists the displacements extracted at the corner point of the top slab, as shown in Fig. 15, which allows a quantitative investigation of the torsion effect during the loading process. A significant torsion effect can be observed at the initial loading, induced by the stiffness difference of the two stiffening walls A and B. This is consistent with the phenomenon exhibited in the experiment (see Table 2). In the numerical prediction, such an effect gradually relieves when the structural capacity reaches the peak, resulting from the cracking in the solid wall B. When approaching the peak load, a wide and horizontal crack occurs at the middle height of the wall, degrading the stiffness of wall B to a level comparable to the wall with an opening. However, such a phenomenon was not observed in the experiment. The structure still presents a significant torsion at the peak load. Such inconsistency should stem from the difference in the cracking pattern of the solid stiffening wall, which

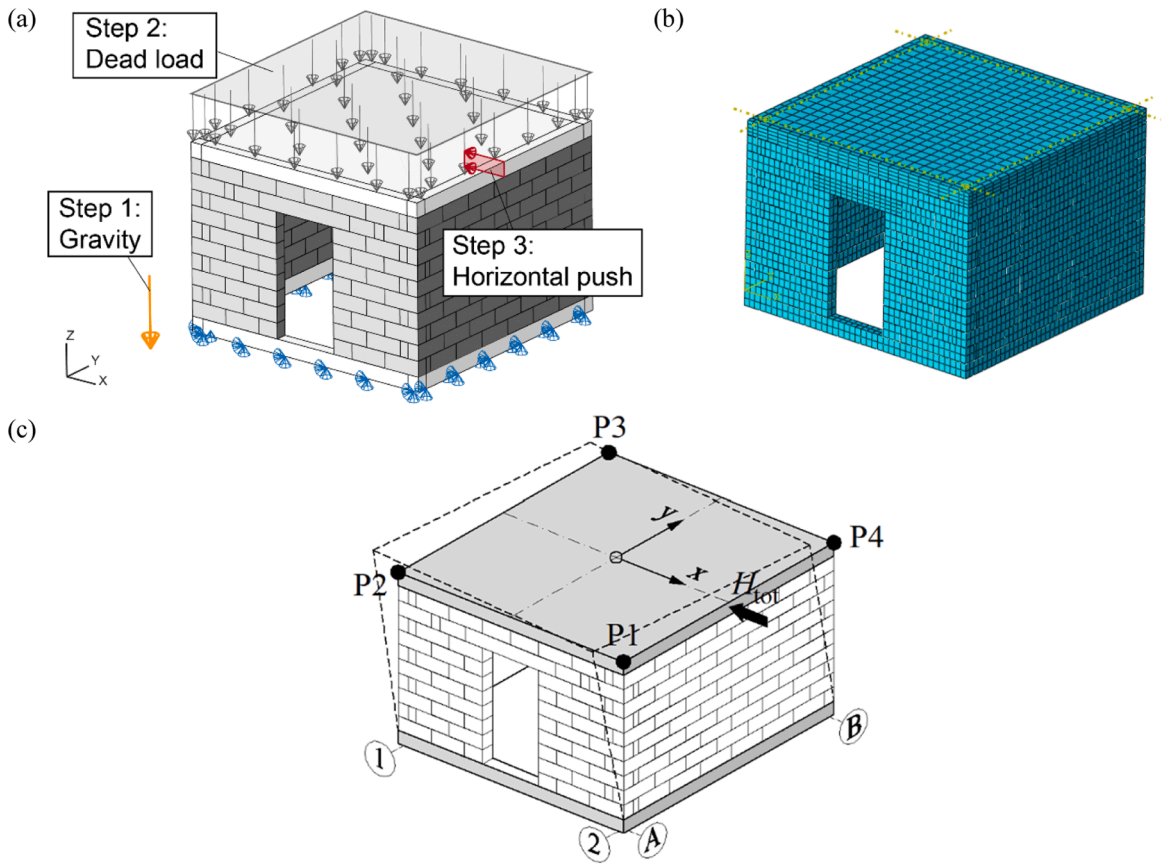

Fig. 15. Finite element model of the AAC walls, Model 2: (a) loads and boundary condition (white cells: concrete beam/slab; grey cells: AAC units), (b) mesh adoption, (c) deformation points.

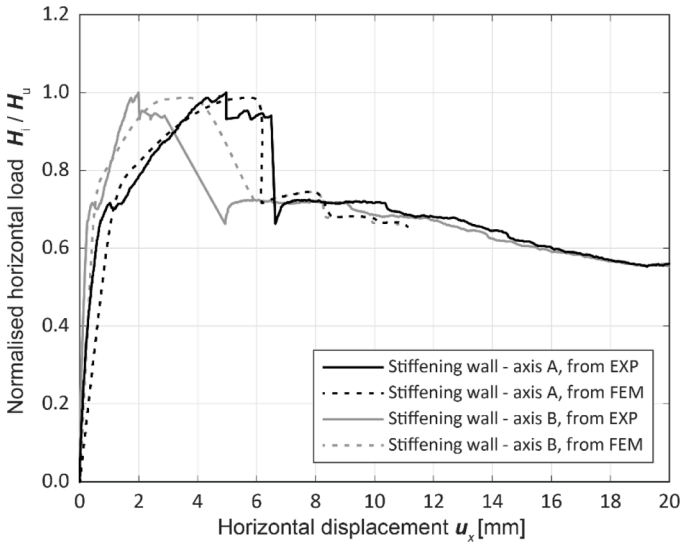

Fig. 16. Comparison of prediction of the calibrated FEM model with the building model 2 (experimental results).

might relate to the inaccuracy of the material parameter estimation. In the experiment, a stepped crack path along the diagonal was exhibited in wall B instead of a long horizontal crack. Therefore, the solid stiffening wall takes full advantage of the cohesion and friction of the joints, bringing about a higher stiffness after cracking happens. Due to the underestimation of the residual stiffness of wall B, the torsion at the post-peak stage even slightly turns to the side of the opening stiffening wall in the numerical simulation. However, the magnitude is not significant compared to the horizontal displacement. Despite the deviation in the deformation mechanism, the magnitude level of these corner displacements agrees well with the experimental measurement.

Fig. 19 demonstrates the distribution of the compressive (minimum) principle stress in the stiffening walls, which is the most critical for the masonry units. Two piers almost carry the load separately in the wall with an opening, since the opening mainly covers the entire building's height. The compression in each wall is translated along the diagonal – Fig. 19(a). Two corners of the opening present a concentration of compressive stress, which agrees with the occurrence of the crack at the early stage. The stress distribution in the solid wall is along the entire diagonal direction, and the stress singularity occurs at the bottom corner (Fig. 19(b)). In the later stage, the stress redistributes due to the crack propagation and concentrates at some blocks at corners or connective regions (Fig. 19(c)–(d)), indicating the crush of the masonry units. Correspondingly, crushing failure or compression-induced cracks in the AAC blocks of those regions can be appreciated in the experiment (Fig. 11).

Regarding the two perpendicular walls, a majorly out-of-plane behaviour can be expected, and the stress distributed along the thickness can thus be very different. The stress distribution on both the inner and outer surfaces is provided below. Wall 1 deforms passively along with the motion of the stiffening walls, and the stress distribution is relatively symmetric (Fig. 20(b)). The stress at the outer surface is constant along the width (Fig. 20(d)). The compression at the bottom is more significant and decreases along the height of the wall. On the inner side, the compressive stress is delivered towards the two bottom corners from the middle-top area (Fig. 20(b)), and such a distribution is analogous to the out-of-plane bending of a plate with three sides fixed. This has implied that the constraint from stiffening walls and bottom

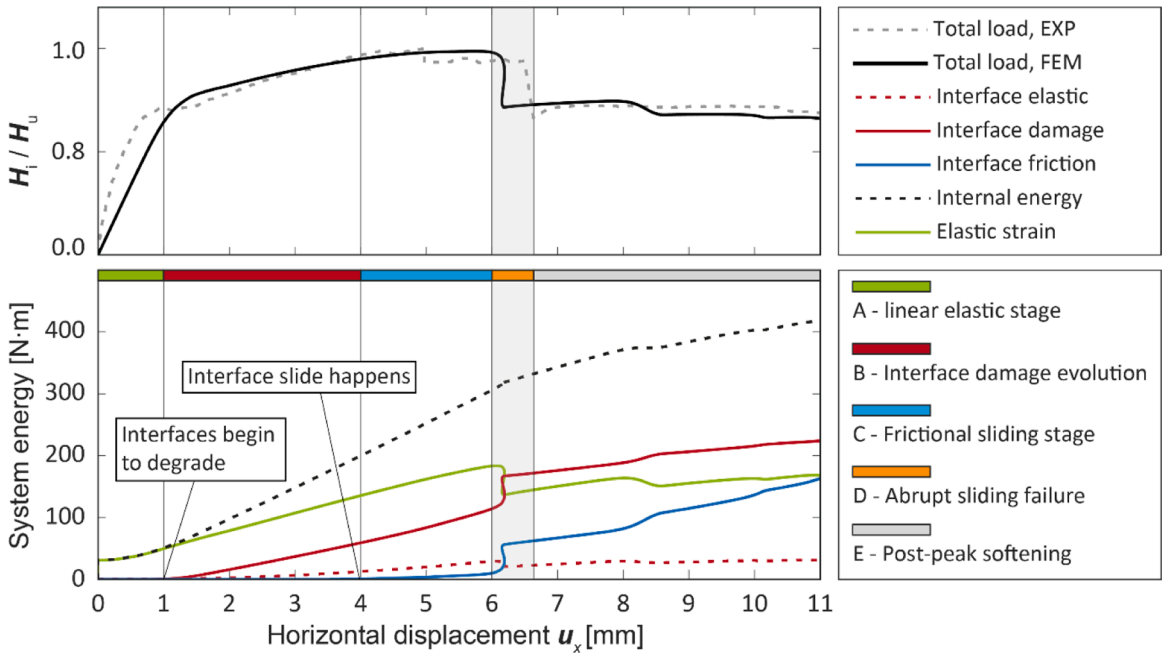

Fig. 17. Energy dissipation of the AAC walls (Model 2) obtained from the calibrated FEM model.

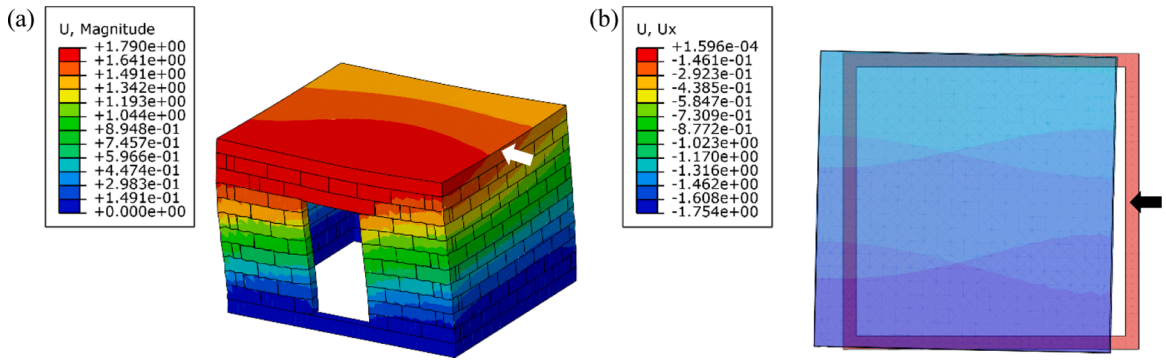

Fig. 18. The deformation of the AAC masonry building (Model 2), $u_x = 1.664$ mm, $H_i = 55.016$ kN: (a) overall perspective, displacement magnitude; (b) top view, displacement along pushing direction.

Table 4
Values of building corners deformations based on FEM.

Point	$H_i = 9.76$ kN		$H_i = H_{cr} = 49.62$ kN		$H_i = H_u = 69.25$ kN		$H_i = H_{res} = 45.89$ kN	
	u_x, mm	u_y, mm	u_x, mm	u_y, mm	u_x, mm	u_y, mm	u_x, mm	u_y, mm
P1	− 0.265	− 0.036	− 1.268	− 0.175	− 5.835	− 0.191	− 11.149	0.302
P2	− 0.217	0.030	− 1.216	0.175	− 5.787	0.240	− 11.077	− 0.201
P3	− 0.156	0.00128	− 0.866	0.156	− 5.345	0.215	− 11.529	− 0.237
P4	− 0.191	− 0.0715	− 0.904	− 0.225	− 5.388	− 0.265	− 11.601	0.222

concrete beams is more critical than that from the top concrete slab. The stress distribution of wall 1 generally remains unchanged during the loading process but becomes more concentrated in some corners and connections between walls (Fig. 20(f) and (h)).

The evolution of the stress distribution in wall 2 during the simulation is more noticeable, which is strongly related to the stiffness variation of the connected stiffening walls. The compression initially appears at the right half of the inner surface (Fig. 20(a)) because this side is connected with the opening wall that presents prominent deformation at the linear elastic stage. The right half of wall 2 thus experiences larger tractive motions. When the external load grows, the solid stiffening wall first reaches the ultimate capacity and begins to crack. The deformation of this wall becomes significant since the stiffness degrades. Therefore, the compressive region of wall 2 gradually transfers to another side close to the solid wall (Fig. 20(e)). The stress distribution at the outer side slightly varies in the simulation, gradually concentrating towards the top corners (Fig. 20(c) and (g)). The compression majorly happens at the top three layers of the blocks, where the distribution along the width is quite uniform. Comparing two perpendicular walls, the stress level of the wall on the loading side is lower than the other one (compare the results of two columns in Fig. 20). The stress concentration predicted in the late loading stage is in line with the occurrence of the cracks observed in the test (Fig. 11).

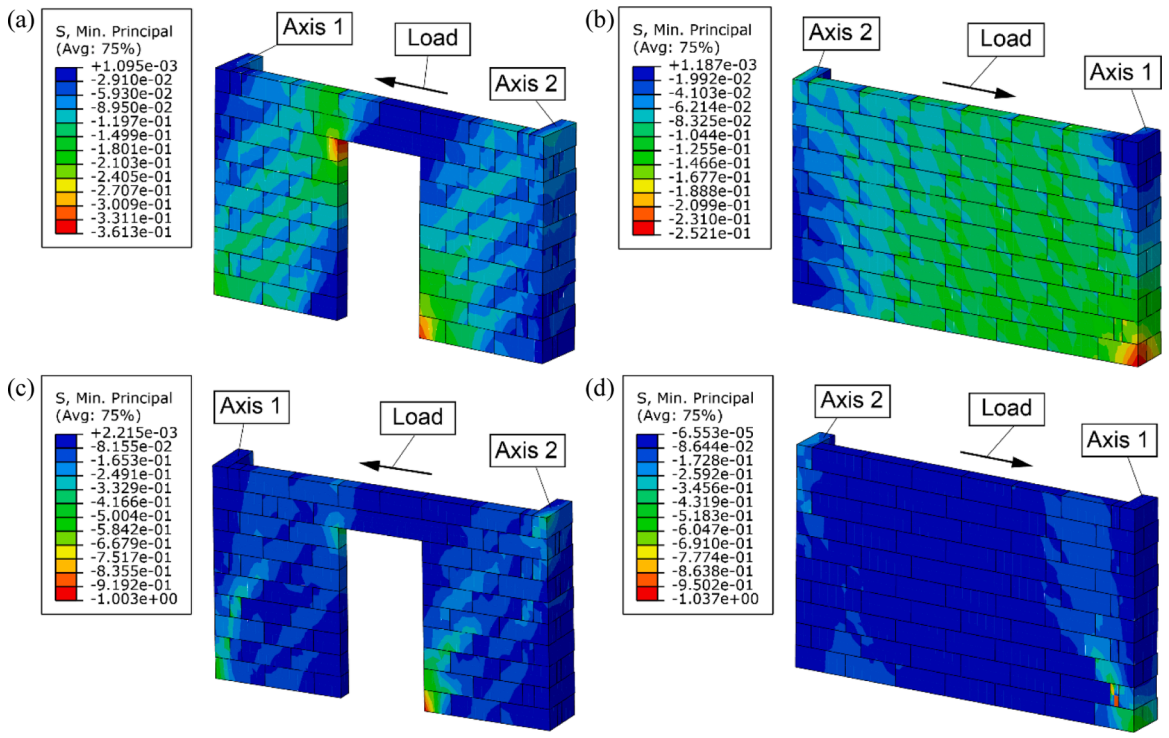

Fig. 19. Stress distribution of the stiffening walls at different load level, minimun principal stress, Model 2: (a) wall A and (b) wall B, $u_x = 1.664$ mm, $H_i = 55.016$ kN; (c) wall A and (d) wall B, $u_x = 9.429$ mm, $H_i = 47.198$ kN.

4.3. Crack propagation

The crack propagation is now compared against the experimental investigations. The cracks that appear during the simulation have been recorded in Fig. 21. Regarding the stiffening wall A, the separation first takes place at the top right corner of the opening due to the concentration effect, and then the mortar at the bottom left of the opening follows to crack (Fig. 21(a)). After that, the top crack enlarged towards the right and finally merged with the vertical separation at the left end of the lintel beam (Fig. 21(b)). This finally triggers the sliding between the first and second layers of the blocks at the left top of the wall, forming a horizontal crack reaching the left edge of the wall (Fig. 21(c)). Such evolution is basically consistent with the experimental observations (see Fig. 11). Meanwhile, several staggered crack propagations are observed at the mid-height of the wall, initiating at the late half of the non-linear increasing stage (Fig. 21(b)). They spread diagonally towards the corner at the post-peak stage (Fig. 21(c)–(d)), weakening the stiffness of the opening wall. These crack propagations are not reported in the experiment, which may be caused by the ignorance of the cohesion of the vertical joint in the numerical modelling. Horizontal sliding is more likely to take place in such modelling.

The degradation of the solid stiffening wall begins at the top left region, where two parallel stepped cracks gradually grow along the diagonal direction (Fig. 22(a)). When the load increases, one further develops downwards until the lower part of the wall (Fig. 22(b)). The sudden horizontal sliding between two layers of the blocks then happens in this region, resulting in the first drop of the load curve (Fig. 22(c)–(d)). Besides, the narrow blocks at the right end separate from the block of the perpendicular wall. The connection of those two walls thus weakens (Fig. 22(a)). Nonetheless, those vertical separations do not further evolve to the left part of the wall during the load process. Only the two short AAC blocks at the right bottom corner exhibit significant rotation at the end of the loading (Fig. 22(d)) due to the extrusion from the abrupt layer-to-layer sliding, and the corresponding vertical separation becomes significant. Comparatively, the propagation of the stepped cracks along the diagonal direction is more notable in the experiment. Some of these cracks also appear in the simulation but are not as clearly defined. No apparent long horizontal sliding occurs in the experiment. Such detailed deviations of the crack propagation may also stem from the simplified consideration of the vertical joint properties. However, the region where cracks appear and their evolution majorly agree well with that reported in the experiment (see Fig. 11).

The cracks of the two perpendicular walls appear at two side ends, typically induced by the passive traction from the stiffening wall. The wall at the loading side cracks at the top part. The deformation of the side connecting with the solid wall is more prominent. One block presents a severe out-of-plane rotation because of the tractive motion (Fig. 23(b)). On the other hand, a torsional sliding failure occurs when connecting the opening wall. The failure of wall 1 primarily occurs at the bottom (Fig. 23(a)), indicating an out-of-plane bending behaviour of the entire wall. The side linked with the solid wall also experienced more significant damage, with both torsion and crush observed. The cracks at the other side of the wall are typically induced by moderate out-of-plane torsion. In the experiment, the occurrence of inter-layer was not appreciated. Most of the failure happens in the AAC block, whereas the region aligns with the predicted cracking and stress concentration area (see Fig. 11).

Therefore, it can be concluded that this calibrated numerical model can reflect the behaviour of the building in the experiment to some extent, and the information retrieved from this model corresponds to the events occurring during the experimental loading. In the discussion, this model will be used to investigate the redistribution of internal forces in the four walls during the loading process to better understand their effects at different stages.

5. Discussion

5.1. Analytical method for horizontal load distribution

An empirical method is proposed to determine the internal forces in shear walls – Fig. 24. The fundamental assumptions of this method are as follows:

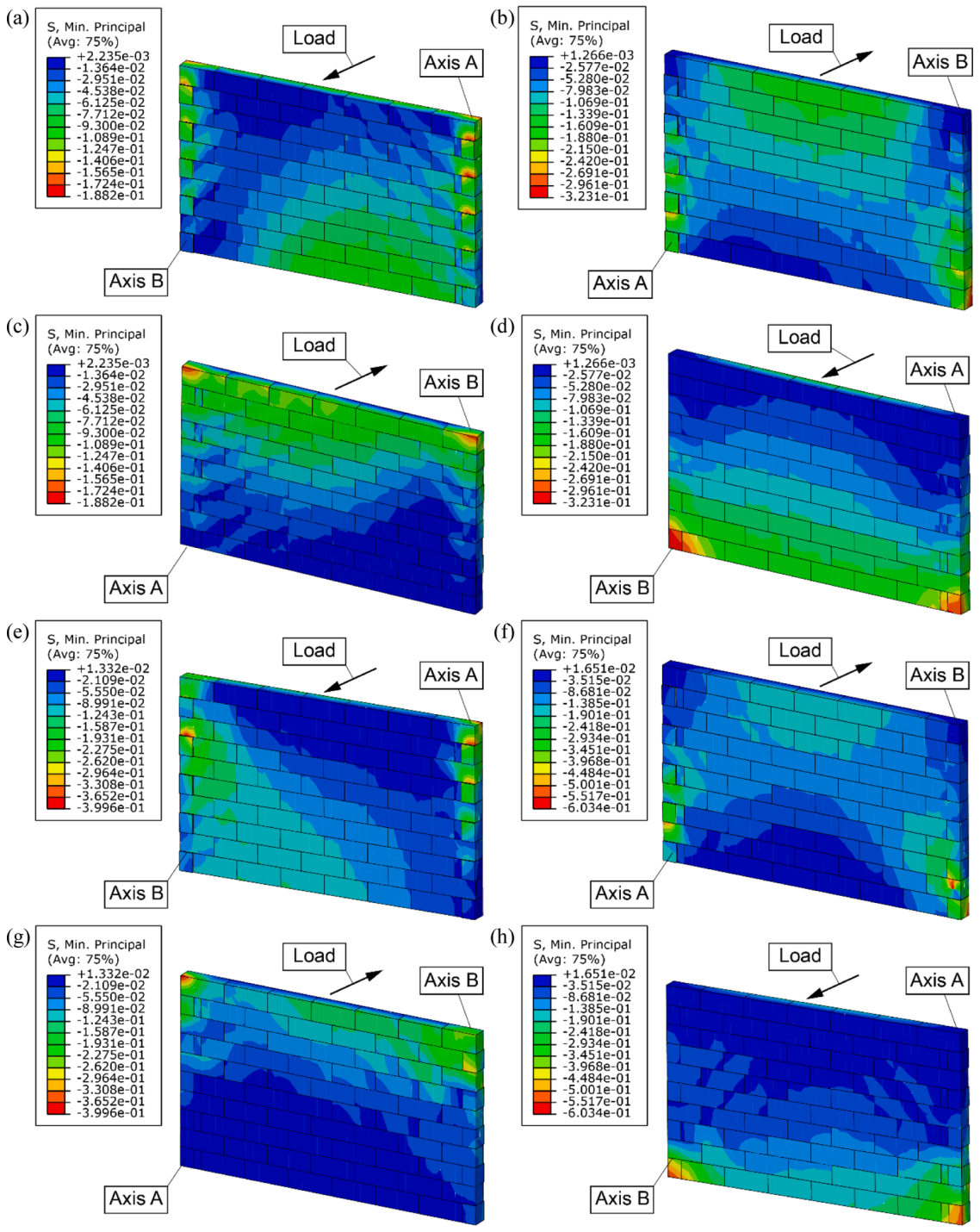

Fig. 20. Stress distribution of the perpendicular walls at different load level, minimun principal stress, Model 2: (a) wall 2 (outer surface), (b) wall 1 (outer surface), (c) wall 2 (inner surface), and (d) wall 1 (inner surface), $u_x = 3.153$ mm, $H_i = 62.659$ kN; (e) wall 2 (outer surface), (f) wall 1 (outer surface), (g) wall 2 (inner surface), (h) wall 1 (inner surface), $u_x = 9.429$ mm, $H_i = 47.198$ kN.

1. The horizontal load acting on the building is taken only by the stiffening walls parallel to the direction of the load.
2. Walls perpendicular to the stiffening walls do not contribute to resisting the external horizontal load.
3. The load acting on the building is assumed to be applied at the loading centre (LC), which coincides with the rotation centre (RC).
4. The walls' displacements are assumed to be parallel to the load direction, and the rotation effect is neglected at the maximum force.
5. The effect of rotation in the elastic and failure phases is considered by introducing a correction factor ω, which represents the relation between total shear angles of stiffening walls, determined when reaching the maximum load H_u.

In general, the stiffness of a masonry wall is defined as the ratio of the total load applied to the wall and its corresponding displacement.

$$K = \frac{H}{\Delta} = \frac{H}{\Theta h} \tag{1}$$

Where:

H – force acting on the wall,

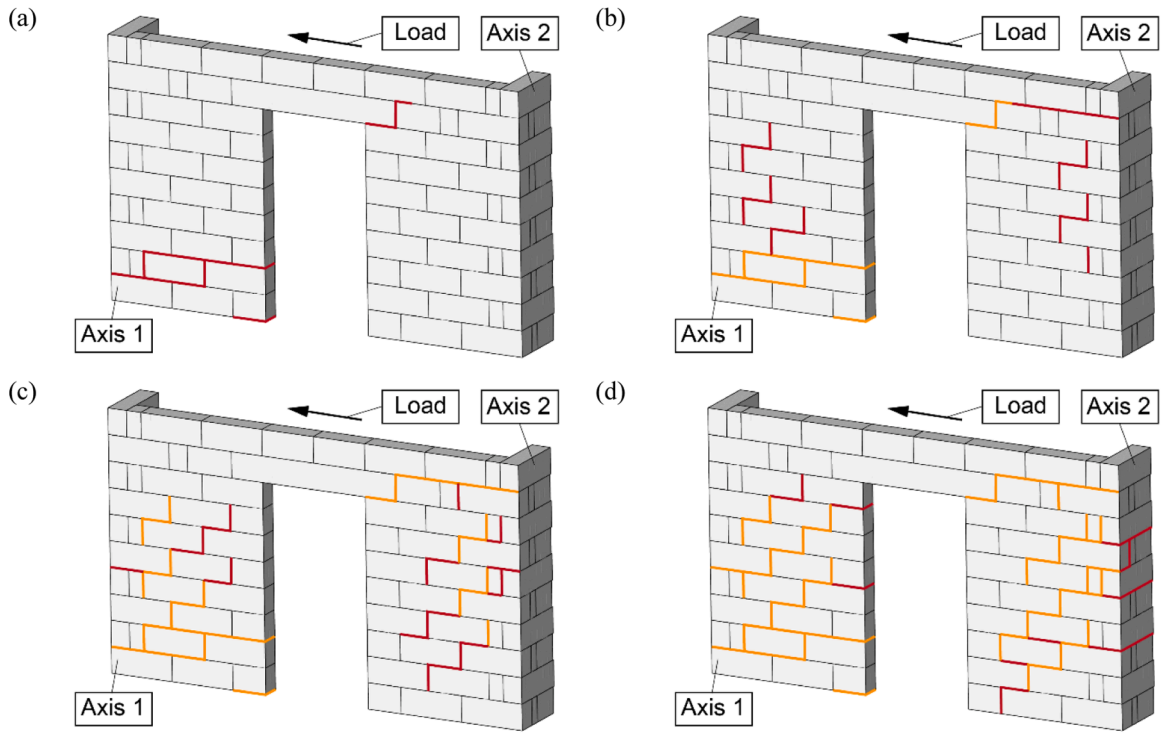

Fig. 21. Crack propagation of the stiffening wall A in Model 2 (red/orange line for new/old cracks): (a) $u_x = 1.994$ mm, $H_i = 56.803$ kN; (b) $u_x = 3.780$ mm, $H_i = 65.044$ kN; (c) $u_x = 5.718$ mm, $H_i = 68.355$ kN, peak load; (d) $u_x = 10.876$ mm, $H_i = 46.042$ kN.

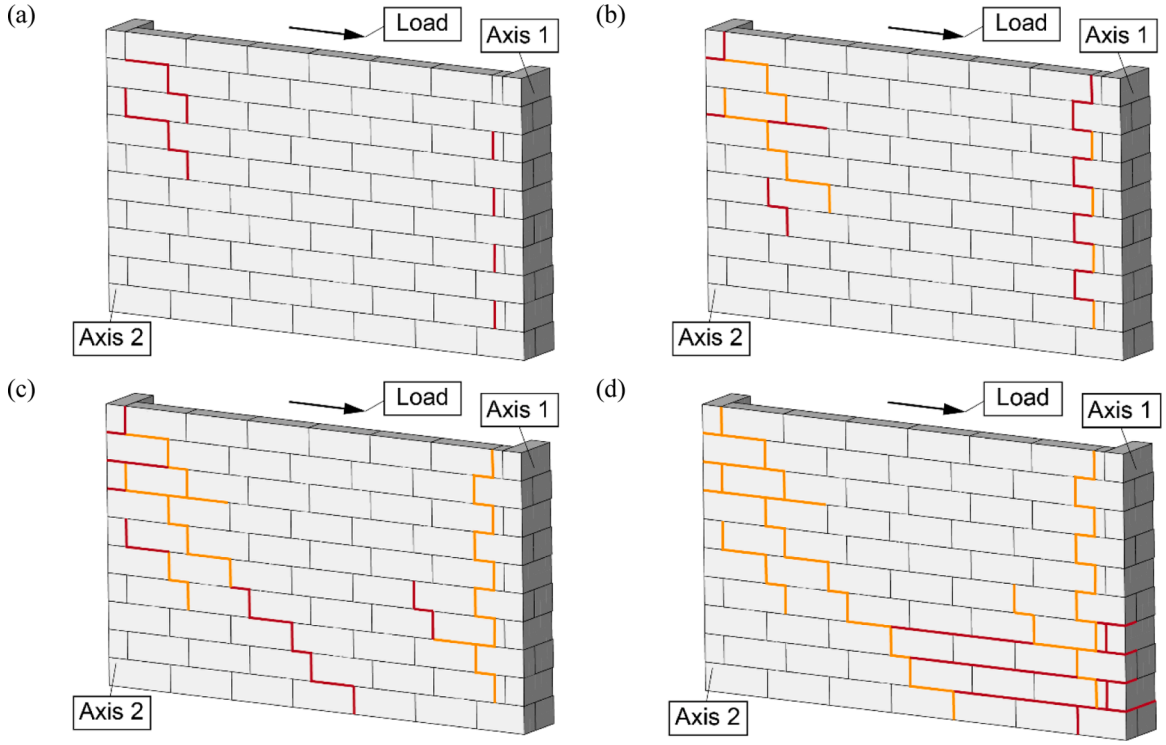

Fig. 22. Crack propagation of the stiffening wall B in Model 2 (red/orange line for new/old cracks): (a) $u_x = 1.994$ mm, $H_i = 56.803$ kN; (b) $u_x = 3.780$ mm, $H_i = 65.044$ kN; (c) $u_x = 5.718$ mm, $H_i = 68.355$ kN, peak load; (d) $u_x = 10.876$ mm, $H_i = 46.042$ kN.

Δ – displacement of the wall,
Θ – shear deformation angle,
h – the height of the wall.
The overall stiffness of the building can be determined by:

$$K_{tot} = \frac{H_{tot}}{\Delta_{tot}} = \frac{H_{tot}}{\Theta_{mv} h} \tag{2}$$

in which:

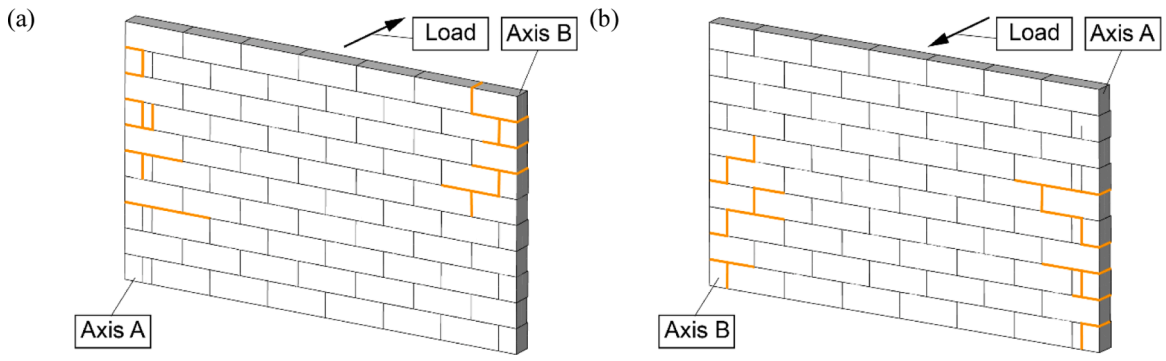

Fig. 23. Crack propagation of the perpendicular walls in Model 2, $u_x = 10.876$ mm, $H_i = 46.042$ kN: (a) wall 1, (b) wall 2.

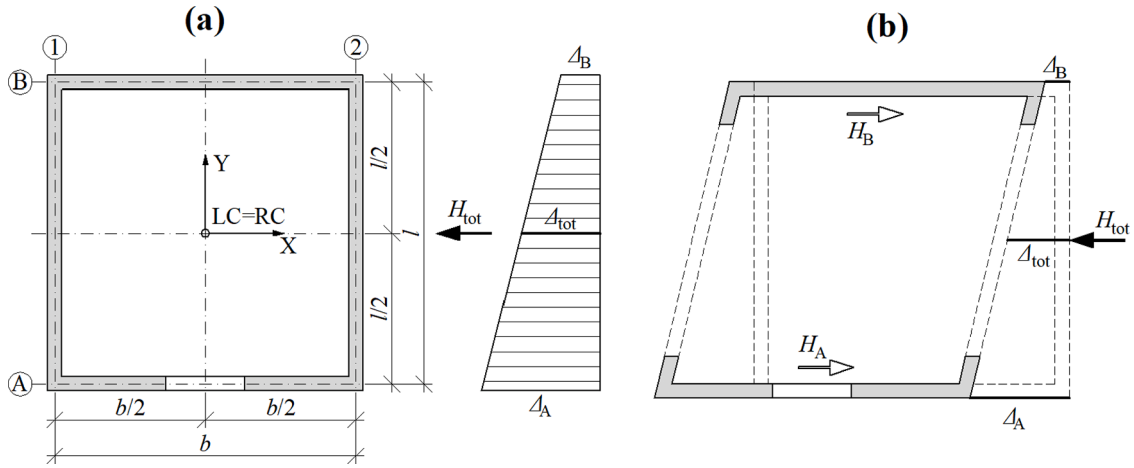

Fig. 24. A graphical representation of the empirical method for determining internal forces in stiffening walls: (a) layout of the building, (b) deformation of the building.

H_{tot} – the total load acting on the building,
Δ_{tot} – the total displacement of the building,
h – the height of the building,
Θ_{mv} – mean value of the shear deformation angle of walls oriented in the direction of the horizontal load, written as:

$$\Theta_{mv} = \frac{\Theta_A + \Theta_B}{2} \tag{3}$$

The forces in the stiffening walls balance the total load acting on the building, and the equilibrium condition is expressed as:

$$H_{tot} = H_A + H_B, \tag{4}$$

which can be expressed as (5):

$$K_{tot}\Delta_{tot} = K_A\Delta_A + K_B\Delta_B \rightarrow K_{tot}\Theta_{mv} = K_A\Theta_A + K_B\Theta_B = K_A\Theta_B\omega + K_B\Theta_B =$$

$$(K_A\omega + K_B)\Theta_B$$

$$\frac{K_{tot}}{(K_A\omega + K_B)} = \frac{\Theta_B}{\Theta_{mv}} \tag{5}$$

Considering that the stiffness of wall B is described by:

$$K_B = \frac{H_B}{\Theta_B h} \rightarrow \Theta_B = \frac{H_B}{K_B h} \tag{6}$$

the value of the force acting on the stiffening wall can be calculated using the relationship (7):

$$\frac{\Theta_B}{\Theta_{mv}} = \frac{K_{tot}}{(K_A\omega + K_B)} \rightarrow \Theta_B = \Theta_{mv}\frac{K_{tot}}{(K_A\omega + K_B)} \rightarrow \frac{H_B}{K_B h} = \Theta_{mv}\frac{K_{tot}}{(K_A\omega + K_B)}$$

$$H_B = K_B h \frac{K_{tot}\Theta_{mv}}{(K_A\omega + K_B)} \tag{7}$$

and the force in wall A can be calculated by:

$$H_A = H_{tot} - H_B = H_{tot} - K_B h \frac{K_{tot}\Theta_{mv}}{(K_A\omega + K_B)} \tag{8}$$

In the specific case where the external load reaches its maximum value, the forces in the walls are equal, as described by:

$$H_{B,u} = K_{B,u} h \frac{K_{tot,u}\Theta_{mv,u}}{(K_{A,u}\omega + K_{B,u})} = \frac{H_{tot,u}}{\Theta_{B,u} h} h \frac{\frac{H_{tot,u}}{\left(\frac{\Theta_{A,u}+\Theta_{B,u}}{2}\right)h}\left(\frac{\Theta_{A,u}+\Theta_{B,u}}{2}\right)}{\left(\frac{H_{tot,u}}{\Theta_{A,u}h}\frac{\Theta_{A,u}}{\Theta_{B,u}} + \frac{H_{tot,u}}{\Theta_{B,u}h}\right)} =$$

$$= \frac{H_{tot,u}}{\Theta_{B,u}} \frac{H_{tot,u}}{h\left(\frac{H_{tot,u}}{\Theta_{A,u}h}\frac{\Theta_{A,u}}{\Theta_{B,u}} + \frac{H_{tot,u}}{\Theta_{B,u}h}\right)} =$$

$$= H_{tot,u}\frac{1}{\Theta_{B,u}} \frac{1}{\left(\frac{1}{\Theta_{A,u}}\frac{\Theta_{A,u}}{\Theta_{B,u}} + \frac{1}{\Theta_{B,u}}\right)} = H_{tot,u}\frac{1}{\Theta_{B,u}} \frac{1}{\left(\frac{1}{\Theta_{B,u}} + \frac{1}{\Theta_{B,u}}\right)} =$$

$$= H_{tot,u}\frac{1}{\Theta_{B,u}} \frac{1}{\frac{2}{\Theta_{B,u}}} = H_{tot,u}\frac{1}{\Theta_{B,u}} \frac{\Theta_{B,u}}{2} = \frac{1}{2}H_{tot,u} \tag{9}$$

In the case of a cracking load, the forces in the walls differ, as shown in a relationship (10).

$$H_{B,cr} = K_{B,cr} h \frac{K_{tot,cr}\Theta_{mv,cr}}{(K_{A,cr}\omega + K_{B,cr})} =$$

$$= \frac{H_{tot,cr}}{\Theta_{B,cr}h}\frac{\frac{H_{tot,cr}}{\left(\frac{\Theta_{A,cr}+\Theta_{B,cr}}{2}\right)h}\left(\frac{\Theta_{A,cr}+\Theta_{B,cr}}{2}\right)}{\left(\frac{H_{tot,cr}}{\Theta_{A,cr}h}\frac{\Theta_{A,u}}{\Theta_{B,u}}+\frac{H_{tot,cr}}{\Theta_{B,cr}h}\right)} =$$

$$= \frac{H_{tot,cr}}{\Theta_{B,cr}}\frac{H_{tot,cr}}{h\left(\frac{H_{tot,cr}}{\Theta_{A,cr}h}\frac{\Theta_{A,u}}{\Theta_{B,u}}+\frac{H_{tot,cr}}{\Theta_{B,cr}h}\right)} =$$

$$= H_{tot,cr}\frac{1}{\Theta_{B,cr}}\frac{1}{\left(\frac{1}{\Theta_{A,cr}}\frac{\Theta_{A,u}}{\Theta_{B,u}}+\frac{1}{\Theta_{B,cr}}\right)} \quad (10)$$

Similarly, in the residual phase, the forces in the walls differ. Following the outlined procedure, the total stiffness and the stiffness of particular walls A and B were calculated. The results are stored in Tables 5 and 6, respectively. The internal forces in the walls were calculated according to the procedure for distributing the horizontal load, which can be found in Table 7.

5.2. Redistribution of internal forces

In this subsection, the internal forces of the building's four walls (Table 8) are extracted from the calibrated numerical model to investigate their evolution during horizontal pushing (Figs. 25 and 26). As expected, the stiffening walls play a significant role in bearing the horizontal load. At the initial stage, the internal force of the solid stiffening wall is 42.9 % higher than that of the opening wall because of the stiffness difference. Before reaching the peak, the force of this wall grows with an analogous trend to that of the total load but with an abrupt decrease after the occurrence of sliding. The residual capacity typically remains flat in the post-peak stage. In contrast, the increase of the internal force in wall A is not halted due to the degradation of the solid wall, which keeps a moderate increase after the linear elastic stage until the end of the simulation, except for several slight drops induced by local slips. The internal force of two perpendicular walls is below 20 % of that of the stiffening walls. The passive-moved wall (wall 1) comparatively takes responsibility for more external load, with a slow but continuous rise after the linear elastic stage. The force of wall 2 is always the lowest during the simulation. It increases initially but soon drops after the cracking of two stiffening walls, with a slight variation.

The proposed simplified analytical method uses empirical results of the shear deformation angles to distribute horizontal loads to the stiffening walls (Table 7). However, a validated numerical model will be used to analyse the redistribution of internal forces. As a result of the progressive cracking process of the walls, there is a change in the internal forces, which arise from the changes in their stiffness. This phenomenon is graphically presented in Fig. 25. A redistribution factor ρ_{red} is introduced to determine the magnitude of the redistribution, which is the ratio of the plastic force at a given load level to the elastic force (Formula (11)). The determination of the elastic internal forces in the walls was based on the force results obtained at a low load level – in the initial phase (Table 8).

Table 6
Stiffness of stiffening walls based on the test.

Model	Model wall	Initial phase $K_{cr,1}$, kN/mm	Elastic phase K_{cr}, kN/mm		Nonlinear phase K_u, kN/mm	Post-peak residual phase K_{res}, kN/mm
2	A	187.60	48.48		13.93	6.92
	B	–	116.36		34.82	9.31
8	A	–	176.87		29.12	17.57
	B	–	170.20		47.41	19.64
9	A	–	536.29[a]	657.50[b]	20.07	16.48
	B	–	226.15[a]	510.30[b]	19.60	17.58

[a] Value calculated for the cracking force of wall A equal to 65.78 kN.
[b] Value calculated for the cracking force of wall B equal to 60.57 kN.

Table 7
Loads of particular stiffening walls based on the test.

Model	Model wall	Elastic phase H_{cr}, kN		Nonlinear phase H_u, kN
8	A	33.23		32.76
	B	19.64		32.76
	ω_u	1.63		
9	A	45.94[a]	33.75[b]	44.33
	B	19.84[a]	26.82[b]	44.33
	ω_u	0.98		

[a] Value calculated for the cracking force of wall A equal to 65.78 kN.
[b] Value calculated for the cracking force of wall B equal to 60.57 kN.

Table 8
The values of internal forces based on FEM.

Internal forces in walls	The internal force in walls at a particular loading stage			
	$H_{i.cr.1.num}$ (initial phase)	$H_{i.pl.cr.num}$	$H_{i.pl.u.num}$	$H_{i.pl.res.1.num}$
H_A, kN	4.103	18.143	25.772	21.827
H_B, kN	6.021	27.888	35.329	16.436
H_1, kN	− 0.909	− 4.438	− 4.445	2.498
H_2, kN	0.84	4.425	4.541	− 1.231

Table 9
The values of elastic internal forces based on FEM.

Stiffening wall	$H_{i.cr.1.num}/H_{cr.1.tot}$	$H_{i.el.cr.num}$	$H_{i.el.u.num}$	$H_{i.el.res.num}$
A	0.41	18,655	24,763	15,507
B	0.59	27,376	36,338	22,756

$$\rho_{red} = \frac{H_{i.pl}}{H_{i.el}} \quad (11)$$

The comparison of the ratios of plastic and elastic forces in shear walls A and B enabled the determination of force redistribution at each load level (Table 10). The redistribution of internal forces at the moment

Table 5
The total stiffness of tested buildings.

Model	Elastic phase				Nonlinear phase		Post-peak residual phase	
	$\Theta_{cr,mv}$ mrad		$K_{tot,cr,1}$, kN/mm		$\Theta_{u,mv}$ mrad	$K_{tot,u}$, kN/mm	$\Theta_{res,mv}$ mrad	$K_{tot,res}$, kN/mm
2	0.28		68.44		1.32	19.90	2.20	7.94
8	0.12		173.47		0.69	36.08	1.22	18.55
9	0.08[a]	0.04[b]	318.1[a]	574.62[b]	1.70	19.83	1.85	17.01

[a] Value calculated for the cracking force of wall A equal to 65.78 kN.
[b] Value calculated for the cracking force of wall B equal to 60.57 kN.

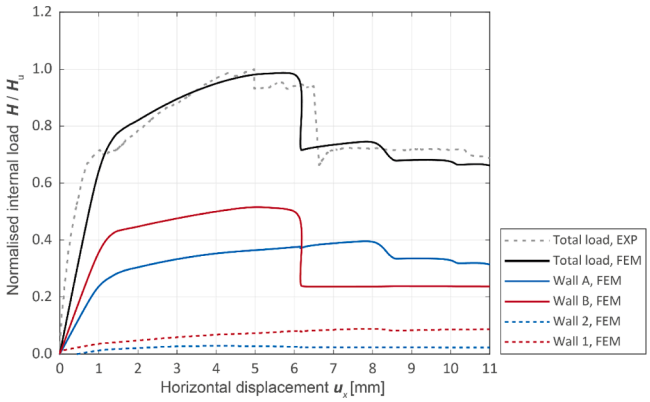

Fig. 25. Variation of the internal force of stiffening and perpendicular walls in Model 2 during the loading.

of cracking is 3 % in wall A and 2 % in wall B. In the nonlinear phase, the redistribution values are higher, at 4 % and 3 %, respectively. Only in the residual phase, where large deformations occur, does the redistribution of internal forces reach 29 % for wall A and 38 % for wall B.

Referring to the provisions of Eurocode 6 [38], which permit design considering a redistribution of forces up to 15 % based on research and advanced numerical modelling, it is argued that these provisions are controversial. However, it should be noted that the standard itself does not define the understanding of the redistribution phenomenon. Allowing such a large change in internal forces in practice requires significant deformations in the structure, which, considering the specifics of the masonry, leads to the structure being already damaged. A correct design of shear walls cannot be limited solely to meeting the ultimate limit state conditions (ULS). It is necessary to limit the permissible levels of deformations and wall displacements.

6. Conclusions

This paper presents three full-scale studies of masonry buildings to demonstrate internal force redistribution and explain the crack propagation process. Since the direct measurement of internal forces in walls is impossible through testing, a numerical model of a selected building

Table 10
The values of the redistribution ratio.

Stiffening wall	Redistribution ratio		
	Elastic phase	Nonlinear phase	Residual phase
A	1.03	0.96	0.71
B	0.98	1.03	1.38

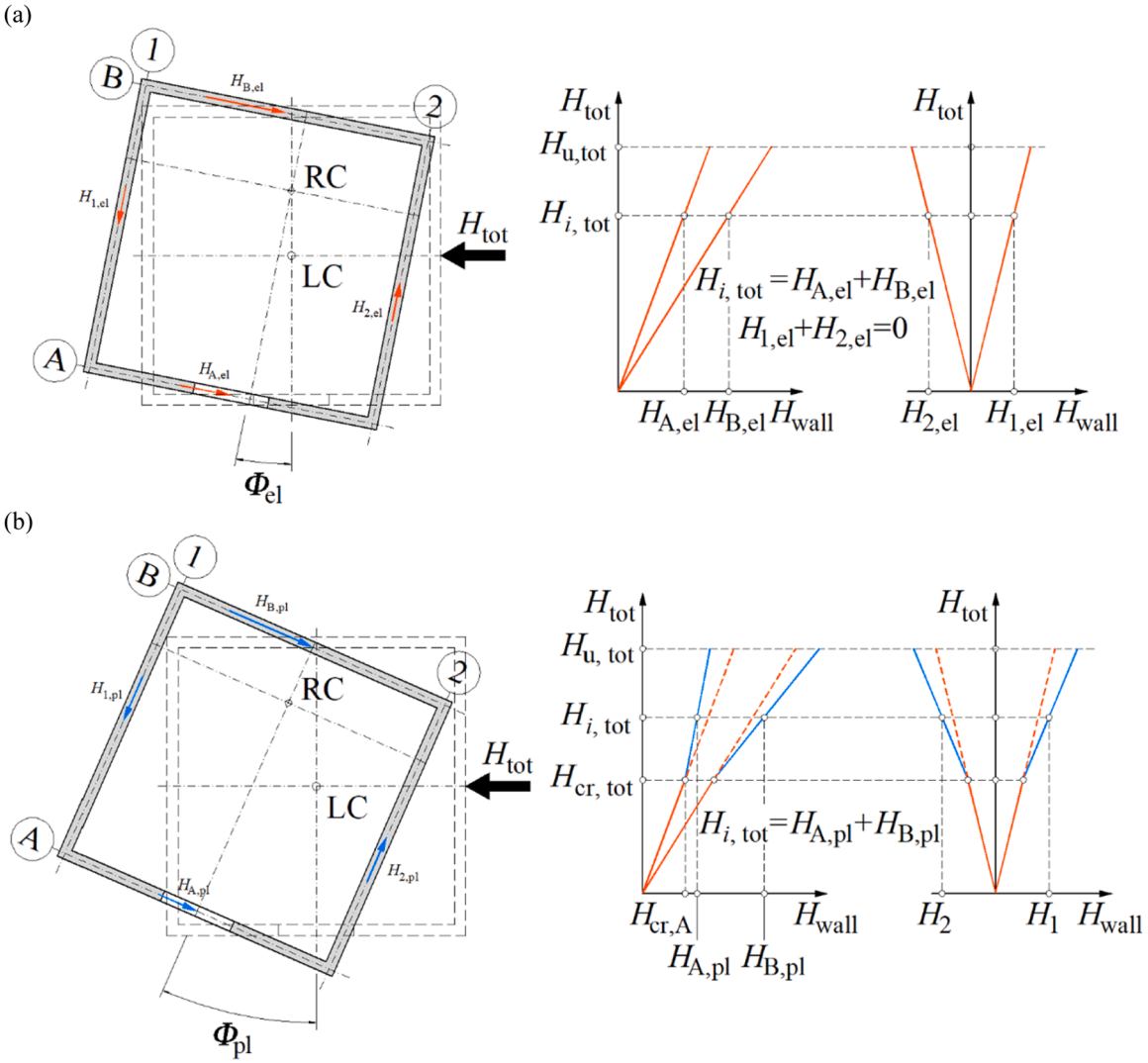

Fig. 26. Graphical interpretation of redistribution phenomenon: (a) linear phase, (b) nonlinear phase.

with a door opening was created to determine the changes in forces. Based on the following research, it is concluded that:

- The European standard for the design of masonry structures, Eurocode 6, allows for the design with redistribution of internal forces in masonry shear walls up to 15 %. However, the standard does not provide a precise definition or propose a method for accounting for this phenomenon.
- All three tested buildings subjected to horizontal loading developed cracks along the diagonals of the shear walls. The cracks passed through the bed and head joints due to the relatively low level of compressive stresses $\sigma_c = 0.05\ N/mm^2$. Crushing of the masonry units was also observed in the compressed corners.
- The tests on the building model, in which a door opening was made in one of the shear walls, showed a rotation of the structure due to the varying stiffness of the walls. In the elastic phase, the displacements of wall with an opening (A) are 2.4 times greater compared to the solid stiffening wall B ($\Theta_{cr.M2.A}/\Theta_{cr.M2.B} = 2.40$)
- The proposed simplified analytical method allows for the distribution of horizontal load to the shear walls, given the known deformation values of the walls.
- Based on a validated numerical building model, the magnitude of redistribution at the cracking moment is 3 % in wall A and 2 % in wall B. In the nonlinear phase, the redistribution values are higher, at 4 % and 3 %, respectively.
- In post-peak behaviour, when more significant deformations occur, the redistribution of internal forces reaches 29 % for wall A and 38 % for wall B.
- Further research is required regarding redistributing internal forces in masonry shear walls. Studies should be conducted on full-scale models of buildings made of different types of masonry units and mortar. It is also recommended to analyse the behaviour of the masonry building subjected to a higher level of prestressing.

CRediT authorship contribution statement

Krzysztof Grzyb: Writing – original draft, Software, Resources, Investigation, Formal analysis, Data curation, Conceptualization, Validation, Visualization. **Gabriele Milani:** Writing – review & editing, Supervision, Methodology. **Yiwei Hua:** Writing – original draft, Visualization, Validation, Software, Investigation, Formal analysis, Data curation, Resources. **Radosław Jasiński:** Writing – review & editing, Visualization, Supervision, Methodology, Investigation, Resources, Software, Validation.

Declaration of Competing Interest

The authors declare that they have no known competing financial interests or personal relationships that could have appeared to influence the work reported in this paper.

The authors declare no potential conflict of interest.

Acknowledgements

The authors thank the technical staff: Krzysztof Jonderko, Marek Niewiadomski, and Wojtek Szczeciński and the companies SOLBET and KONBET for fruitful collaboration in supplying building materials for the research.

Yiwei Hua would also like to thank the China Scholarship Council (CSC) for its financial support under grant CSC No. 202108320019.

Disclosure statement

The author Gabriele Milani is an editor of this journal. In accordance with policy, Gabriele Milani was blinded to the entire peer review process.

Data availability

Data will be made available on request.

References

[1] Massart TJ, Peerlings RHJ, Geers MGD. Mesoscopic modeling of failure and damage-induced anisotropy in brick masonry. Eur J Mech A-Solids 2004;23(5):719–35. https://doi.org/10.1016/j.euromechsol.2004.05.003.
[2] Dhanasekar M, Page A, Kleeman P. The failure of brick masonry under biaxial stresses. Proc Inst Civ Eng 1985;79(2):295–313. https://doi.org/10.1680/iicep.1985.992.
[3] Shabdin M, Zargaran M, Attari NKA. Experimental diagonal tension (shear) test of Un-Reinforced Masonry (URM) walls strengthened with textile reinforced mortar (TRM). Constr Build Mater 2018;164:704–15. https://doi.org/10.1016/j.conbuildmat.2017.12.234.
[4] Krejčí T, Koudelka T, Bernardo V, Šejnoha M. Effective elastic and fracture properties of regular and irregular masonry from nonlinear homogenization. Comput Struct 2021;254:106580. https://doi.org/10.1016/j.compstruc.2021.106580.
[5] Bean Popehn JR, Schultz AE. Influence of imperfections on the out-of-plane flexural strength of post-tensioned masonry walls. Constr Build Mater 2013;41:942–9. https://doi.org/10.1016/j.conbuildmat.2012.07.016.
[6] Lim W-Y. Experimental investigation of size effect on unreinforced concrete brick masonry walls under in-plane shear loading. Constr Build Mater 2024;428:136346. https://doi.org/10.1016/j.conbuildmat.2024.136346.
[7] Dauda JA, Iuorio O, Muhit IB, Da Silva LCM. Systematic review of experimental testing of masonry walls' failure: comparative analysis and future directions. Eng Fail Anal 2024;163:108571. https://doi.org/10.1016/j.engfailanal.2024.108571.
[8] Paevere PJ, Foliente GC, Kasal B. Load-Sharing and Redistribution in a one-story woodframe building. J Struct Eng 2003;129(9):1275–84. https://doi.org/10.1061/(ASCE)0733-9445(2003)129:9(1275).
[9] Phillips TL, Itani RY, McLean DI. Lateral load sharing by diaphragms in wood-framed buildings. J Struct Eng 1993;119(5):1556–71. https://doi.org/10.1061/(ASCE)0733-9445(1993)119:5(1556).
[10] Li Z, He M, Lam F, Li M. Load-sharing mechanism in timber-steel hybrid shear wall systems. Front Struct Civ Eng 2015;9(2):203–14. https://doi.org/10.1007/s11709-015-0293-y.
[11] Borah B, Kaushik HB, Singhal V. Seismic force distribution in members of confined masonry buildings. Eng Struct 2022;266:114605. https://doi.org/10.1016/j.engstruct.2022.114605.
[12] Li L, Zheng W, Wang Y. Review of moment redistribution in statically indeterminate RC members. Eng Struct 2019;196:109306. https://doi.org/10.1016/j.engstruct.2019.109306.
[13] Aydogan MS, Aydemir C, Arslan G. Moment redistribution in continuous reinforced concrete beams: experimental study and analytical investigation. Structures 2024;63:106440. https://doi.org/10.1016/j.istruc.2024.106440.
[14] Baša N, Kopitović Vuković N, Ulićević M, Muhadinović M. Effects of internal force redistribution on the limit states of continuous beams with GFRP reinforcement. Appl Sci 2020;10(11):3973. https://doi.org/10.3390/app10113973.
[15] L.H. Lee, S.T. Quek, K.K. Ang. Moment redistribution in continuous profiled steel–concrete composite slabs.
[16] Chen S, Jia Y. Required and available moment redistribution of continuous steel–concrete composite beams. J Constr Steel Res 2008;64(2):167–75. https://doi.org/10.1016/j.jcsr.2007.05.006.
[17] Gattesco N, Macorini L, Fragiacomo M. Moment redistribution in continuous steel-concrete composite beams with compact cross section. J Struct Eng 2010;136(2):193–202. https://doi.org/10.1061/(ASCE)ST.1943-541X.0000098.
[18] Tao M-X, Wang Y-L, Zhao J-Z. Internal force redistribution caused by cracking of concrete in composite frame structures under lateral load. Eng Struct 2023;283:115876. https://doi.org/10.1016/j.engstruct.2023.115876.
[19] Mahmood SMF, Foster SJ, Valipour H. Moment redistribution and post-peak behaviour of lightly reinforced-SFRC continuous slabs. Eng Struct 2021;232:111834. https://doi.org/10.1016/j.engstruct.2020.111834.
[20] Oehlers DJ, Ju G, Liu IST, Seracino R. Moment redistribution in continuous plated RC flexural members. Part 1: neutral axis depth approach and tests. Eng Struct 2004;26(14):2197–207. https://doi.org/10.1016/j.engstruct.2004.08.003.
[21] Einpaul J, Fernández Ruiz M, Muttoni A. Influence of moment redistribution and compressive membrane action on punching strength of flat slabs. Eng Struct 2015;86:43–57. https://doi.org/10.1016/j.engstruct.2014.12.032.
[22] Nethercot DA, Li TQ, Choo BS. Required rotations and moment redistribution for composite frames and continuous beams. J Constr Steel Res 1995;35(2):121–63. https://doi.org/10.1016/0143-974X(94)00037-I.
[23] Christou G, Hegger J, Classen M. Multi-span composite girders with composite dowels – experimental investigations and design approach to account for the beneficial effect of shear force redistribution along the composite interface. Eng Struct 2023;285:115944. https://doi.org/10.1016/j.engstruct.2023.115944.
[24] Salmanpour AH, Mojsilović N, Schwartz J. Displacement capacity of contemporary unreinforced masonry walls: An experimental study. Eng Struct 2015;89:1–16. https://doi.org/10.1016/j.engstruct.2015.01.052.
[25] Farshchi DM, Motavalli M, Schumacher A, Marefat MS. Numerical modelling of in-plane behaviour of URM walls and an investigation into the aspect ratio, vertical and horizontal post-tensioning and head joint as a parametric study. Arch Civ Mech Eng 2009;9(1):5–27. https://doi.org/10.1016/S1644-9665(12)60037-5.

[26] Liu Z, Crewe A. Effects of size and position of openings on in-plane capacity of unreinforced masonry walls. Bull Earthq Eng 2020;18(10):4783–812. https://doi.org/10.1007/s10518-020-00894-0.
[27] Hwang S-H, Kim S, Yang K-H. In-plane lateral load transfer capacity of unreinforced masonry walls considering presence of openings. J Build Eng 2022;47:103868. https://doi.org/10.1016/j.jobe.2021.103868.
[28] Calderón S, Sandoval C, Inzunza E, Cruz-Noguez C, Rahim AB, Vargas L. Influence of a window-type opening on the shear response of partially-grouted masonry shear walls. Eng Struct 2019;201:109783. https://doi.org/10.1016/j.engstruct.2019.109783.
[29] Vargas L, Sandoval C, Bertolesi E, Calderón S. Seismic behavior of partially grouted masonry shear walls containing openings: experimental testing. Eng Struct 2023;278:115549. https://doi.org/10.1016/j.engstruct.2022.115549.
[30] Jasinski R. Effects of opening shapes on behaviour of shear walls made of AAC masonry units. IOP Conf Ser Mater Sci Eng 2019;471:022011. https://doi.org/10.1088/1757-899X/471/2/022011.
[31] Howlader MK, Masia MJ, Griffith MC. Numerical analysis and parametric study of unreinforced masonry walls with arch openings under lateral in-plane loading. Eng Struct 2020;208:110337. https://doi.org/10.1016/j.engstruct.2020.110337.
[32] Paparo A, Beyer K. Quasi-static cyclic tests of two mixed reinforced concrete–unreinforced masonry wall structures. Eng Struct 2014;71:201–11. https://doi.org/10.1016/j.engstruct.2014.04.002.
[33] Nakamura Y, Derakhshan H, Magenes G, Griffith MC. Influence of diaphragm flexibility on seismic response of unreinforced masonry buildings. J Earthq Eng 2017;21(6):935–60. https://doi.org/10.1080/13632469.2016.1190799.
[34] Kollerathu JA, Menon A. Role of diaphragm flexibility modelling in seismic analysis of existing masonry structures. Structures 2017;11:22–39. https://doi.org/10.1016/j.istruc.2017.04.001.
[35] Betti M, Galano L, Vignoli A. Comparative analysis on the seismic behaviour of unreinforced masonry buildings with flexible diaphragms. Eng Struct 2014;61:195–208. https://doi.org/10.1016/j.engstruct.2013.12.038.
[36] Sajid HU, Ashraf M, Ali Q, Sajid SH. Effects of vertical stresses and flanges on seismic behavior of unreinforced brick masonry. Eng Struct 2018;155:394–409. https://doi.org/10.1016/j.engstruct.2017.11.013.
[37] Chen X, Liu Y. A finite element study of the effect of vertical loading on the in-plane behavior of concrete masonry infills bounded by steel frames. Eng Struct 2016;117:118–29. https://doi.org/10.1016/j.engstruct.2016.03.010.
[38] PN-EN 1996-1-1:2023-08. Eurocode 6 – design of masonry structures – Part 1-1: general rules for reinforced and unreinforced masonry structures.
[39] Grzyb K, Jasiński R. Research on the behavior of stiffening walls in single-storey buildings made of autoclaved aerated concrete (AAC) masonry units. Materials 2022;15(20):7404. https://doi.org/10.3390/ma15207404.
[40] I. Caliò, M. Marletta, B. Pantò. A simplified model for the evaluation of the seismic behaviour of masonry buildings. Presented at the Tenth International Conference on Civil, Structural and Environmental Engineering Computing, Rome, Italy. p. 195. ⟨https://doi.org/10.4203/ccp.81.195⟩.
[41] Szabó S, Funari MF, Lourenço PB. Masonry patterns' influence on the damage assessment of URM walls: current and future trends. Dev Built Environ 2023;13:100119. https://doi.org/10.1016/j.dibe.2023.100119.
[42] Milani G, Bucchi A. Kinematic FE homogenized limit analysis model for masonry curved structures strengthened by near surface mounted FRP bars. Compos Struct 2010;93(1):239–58. https://doi.org/10.1016/j.compstruct.2010.05.013.
[43] Zahra T, Thamboo J, Asad M. Compressive strength and deformation characteristics of concrete block masonry made with different mortars, blocks and mortar beddings types. J Build Eng 2021;38:102213. https://doi.org/10.1016/j.jobe.2021.102213.
[44] Deng M, Yang S. Experimental and numerical evaluation of confined masonry walls retrofitted with engineered cementitious composites. Eng Struct 2020;207:110249. https://doi.org/10.1016/j.engstruct.2020.110249.
[45] Ram I, Senderovich S, Brodsky A. Experimental and numerical study on the impact of geometrical and mechanical properties of joints on the out-of-plane behaviour of masonry walls. Structures 2025;75:108849. https://doi.org/10.1016/j.istruc.2025.108849.